International Journal of Thermofluids 22 (2024) 100611

Contents lists available at ScienceDirect

International Journal of Thermofluids

journal homepage: www.sciencedirect.com/journal/international-journal-of-thermofluids

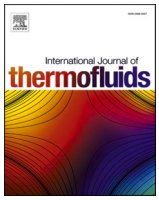

Vibration characteristics of multilayer functionally graded microplates with variable thickness reinforced by graphene platelets resting on the viscoelastic medium under thermal effects

Jintara Lawongkerd [a], Peyman Roodgar Saffari [a,*], Thira Jearsiripongkul [b], Chanachai Thongchom [c], Sikiru Oluwarotimi Ismail [d], Pouyan Roodgar Saffari [c], Suraparb Keawsawasvong [e]

[a] Department of Civil Engineering, Thammasat School of Engineering, Faculty of Engineering, Thammasat University, Pathumthani, 12120, Thailand
[b] Department of Mechanical Engineering, Thammasat School of Engineering, Faculty of Engineering, Thammasat University, Pathumthani, 12120, Thailand
[c] Research Unit in Structural and Foundation Engineering, Department of Civil Engineering, Faculty of Engineering, Thammasat School of Engineering, Thammasat University, Pathumthani, 12120, Thailand
[d] Department of Engineering, School of Physics, Engineering and Computer Science, University of Hertfordshire, Hatfield, AL10 9AB, England, United Kingdom
[e] Research Unit in Sciences and Innovative Technologies for Civil Engineering Infrastructures, Department of Civil Engineering, Faculty of Engineering, Thammasat School of Engineering, Thammasat University, Pathumthani, 12120, Thailand

ARTICLE INFO

Keywords:
Variable thickness
Free vibration
Graphene platelet
Functionally graded microplates
Modified strain gradient theory

ABSTRACT

Due to their improved mechanical properties and adaptability, microplates with tailored variable thickness profiles are becoming essential parts of advanced micro- and nanoelectromechanical systems (MEMS and NEMS). This study conducts a thorough analytical analysis of the vibration properties of thermally loaded, multilayer functionally graded graphene platelet-reinforced composite (FG-GPLRC) microplates of linearly or parabolically varying thickness resting on viscoelastic medium under different boundary conditions. The Halpin–Tsai micromechanical model and the law of mixtures are employed to calculate the effective material characteristics for various reinforcement distributions in the microplate. These distributions encompass uniformly symmetric and asymmetric arrangements. The study utilized the first-order shear deformation theory (FSDT) in conjunction with the modified strain gradient theory (MSGT) and Hamilton's principle to generate the dynamic governing equations for the structure, accounting for size-dependent effects. The resulting equations are afterwards solved using the utilization of the Galerkin technique. This enables the evaluation of the proposed solution's correctness and precision. The impact of various factors on vibration behavior is investigated through numerical analysis. These factors encompass length scale parameters, temperature fluctuations, temperature distribution profiles, boundary conditions, the distribution pattern of the GPL, taper constants in both unidirectional and bidirectional scenarios, the weight fraction of the GPL.

1. Introduction

Structures and structural components that include thickness profiles customized in a spatial manner have attracted significant attention across diverse engineering disciplines owing to their improved mechanical characteristics and ability to perform multiple functions [1]. By changing plate thickness in the in-plane directions, one can optimize stiffness and mass distribution to meet particular requirements in structural design challenges. This facilitates enhanced structural efficiency and significant weight reduction, which is particularly crucial for weight-sensitive applications such as those found in airplanes and spacecraft [2]. Moreover, the utilization of variable-thickness plates and shells offers advantageous customization of structural integrity, vibrational behavior, thermal conduction, heat dissipation, acoustic propagation, and other characteristics within micro- and nanoscale systems. Kumar et al. [3] analyzed the effects of porosity and an orthotropic foundation on free and forced vibrations in a plate of functionally graded material (FGM) of varying thickness lying on an orthotropic foundation.

In recent years, much attention has been paid to microstructures and

* Corresponding author.
E-mail address: rpeyman@engr.tu.ac.th (P. Roodgar Saffari).

https://doi.org/10.1016/j.ijft.2024.100611

Available online 16 February 2024

microplates because of their new properties and numerous potentials uses across a wide range of industries. These microstructures are beneficial for advanced engineering applications because of their improved mechanical, thermal, and acoustic qualities, among other benefits [4,5]. In several disciplines, including electronics, MEMS, and biomedical engineering, microplates are essential for the development of high-performance devices [6,7]. The reliance on conventional continuum mechanics theories has been a prevailing practice in the prediction and understanding of the mechanical behavior of macroscale systems for several decades. However, the application of conventional concepts to structures at the micro and nanoscale presents several limitations and challenges. The primary reason for this is the significant influence of size effects and surface forces, which presents limitations and problems to their application. The constraints imposed by classical continuum mechanics theories in accurately representing size-dependent events at micro- and nanoscales resulted in significant research efforts aimed at formulating non-classical theories. Eringen's nonlocal theory (NT) was a seminal contribution that included long-range interatomic interactions in order to account for the scale effect [8,9]. This inspired various other non-classical formulations like the strain gradient theory (SGT) [10], modified strain gradient theory (MSGT) [11], modified couple stress theory (MCST) [12], and nonlocal strain gradient theory (NSGT) [13]. Each of these concepts has significantly contributed to our understanding of mechanics on the micro- and nanoscale. The NT of Eringen encompasses a comprehensive framework for elasticity that includes the consideration of long-range interactions among atoms. In the context of the NT, it is important to note that the stress at a specific point is influenced by the strain at all points within the material [14–16]. The SGT is an elastic theory that incorporates the influence of strain gradients, which are the spatial derivatives of strain [17]. Using dilatation, deviatoric, and rotational gradient effects independently of one another, the three length scale parameters in MSGT give a more accurate characterization of size effects [18]. The single length scale parameter in MCST incorporates the effects of microstructure and gradients in an average sense, providing improvements over classical continuum theories for small scale structures [19]. The concept of NSGT is a combination of NT and SGT, which aims to describe the mechanical behavior of materials by considering the effects of both nonlocality and strain gradients [20]. A popular computational method used to examine the characteristics of micro- and nanostructures is molecular dynamics (MD). It involves modeling the interactions of individual atoms and molecules. While MD simulations provide valuable insights, their computational requirements are significant, rendering them impractical for large-scale systems [21]. However, non-classical theories offer a more efficient and computationally simpler method to analyze these structures, making them a great option for scientists and engineers. These non-classical theories have been extensively studied in recent years to examine the dynamic response of nano- and micro-plates with uniform and varying thickness profiles [22–27]. Phung-Van et al. [28] developed a scale-dependent NSGT isogeometric model to examine the behavior of metal foam nanoscale plates that have different porosity distributions. Hung et al. [29] used the extended higher-order shear deformation theory and MSGT to investigate the elastic instability and free vibration of magneto-electro-elastic microplates subjected to temperature fluctuations. The small-scale-dependent geometrically nonlinear flexural response of microplates with arbitrary forms and variable thickness composed of FG composites was investigated by Yang et al. [30]. A MCST has been developed, which integrates the von Karman large deflection assumption into a quasi-three-dimensional (quasi-3D) plate framework. Hung et al. [31] employed MSGT in conjunction with higher-order shear deformation plate theory to investigate the vibration problem and buckling behavior of porous metal foam microplates.

Functionally graded materials (FGMs) are a class of engineered materials that possess spatially varying characteristics according to a given gradient function. This enables the customization of mechanical, thermal, electrical, and other attributes in order to enhance overall performance. FGMs find extensive utility across several domains, including the aerospace, automotive, medicinal, and energy sectors [32–36]. The use of carbon nanotubes (CNTs) and composites to reinforce FGMs can further improve their performance. Functionally graded carbon nanotube-reinforced composites (FG-CNTRC) are composite materials that exhibit a gradient in their composition and are reinforced using CNTs [37]. The characteristics of FG-CNTRC may be customized to satisfy certain design specifications by spatially altering the distribution of CNT reinforcements. CNTs exhibit exceptional mechanical qualities and possess high electrical conductivity [38]. It is possible to create lightweight FG-CNTRC with improved strength, stiffness, fracture toughness, thermal conductivity, and electrical characteristics by evenly dispersing the CNTs [39]. Graphene, an allotrope of carbon with a two-dimensional structure, possesses remarkable mechanical, electrical, and thermal characteristics. The incorporation of graphene platelets (GPLs) into FGMs has been shown to significantly enhance their mechanical properties, including strength, stiffness, fracture toughness, fatigue life, and thermal conductivity [40,41]. GPLR-FGMs exhibit exceptional customizable characteristics, remarkable strength-to-weight ratios, and notable resistance to corrosion. These attributes render them very auspicious materials for the implementation of innovative engineering applications in many industries, such as automotive [42], aerospace [43], and biomedical [44]. Nguyen and Lee [45] performed a comprehensive numerical investigation of the static and dynamic characteristics of smart FG microplates that are reinforced with GPLs and subjected to simultaneous mechanical and electrical stresses. The researchers employed a comprehensive numerical model that incorporated refined plate theory (RPT), the MCST, and non-uniform rational B-spline (NURBS)-based isogeometric analysis (IGA) in order to examine the intricate behaviors shown by small-scale structures. Phung-Van et al. [46] introduced a highly effective and direct approach for examining the flexural and natural oscillation characteristics of multilayer FG-GPLRC nanoplates. Their methodology combines RPT with IGA, resulting in a thorough understanding of these intricate structures. Recently, Zhang et al. [47] studied the effects of combined aerodynamic and centrifugal pressures on the nonlinear dynamical characteristics of a composite spinning warping blade reinforced with FG-GPLs. The blade is essentially reduced to a rectangular, cross-sectioned spinning cantilever plate that is FG-GPLs -strengthened. The dynamic model takes into account four distinct GPL distribution patterns over the plate thickness. Based on the higher-order shear deformation theory and NSGT, Phung-Van et al. [48] numerically studied the effect of distributions of GPLs on the free vibration of FG-GPLRC nanoplates.

After conducting a comprehensive review of the existing literature, it is evident that previous studies have primarily focused on investigating the dynamic behavior of FG-GPLRC rectangular plates with uniform thickness. Therefore, the novelty of this work lies in the development of an analytical model based on MSGTFSDT and its application to elucidate the vibration characteristics of FG-GPLRC variable thickness microplates coupled with a viscoelastic foundation and thermal loading, which has not been reported in literature before. The absence of comprehensive research in this area has provided major motivation for the current investigation, which seeks to fill this knowledge gap and enhance our understanding of the intricate relationship between temperature fluctuations and vibration characteristics in microstructures with varying

thickness. In order to compute the effective material properties, the micromechanical model developed by Halpin and Tsai as well as the law of mixtures are utilized. Uniformly distributed (UD), and three distinct forms of FG distribution (FG-A, FG-O, FG-X) are the four new ways that GPLs can be distributed. By utilizing Hamilton's methodology, the governing equation is formulated using the FSDT and subsequently solved using the weighted residual (Galerkin) algorithm. The key novelties that this work presents are as: This is the first study combining MSGT with variable thickness modeling of multilayer composite microplates, enabling size-dependent vibration analysis. The synergistic modifications of graphene platelet reinforcements and thickness tailoring have not been reported for vibration behavior which is analyzed here. The proposed approach presents several advantages. Firstly, it excels in capturing size-dependent vibrational behavior by employing strain gradient modeling. Additionally, it offers enhanced design flexibility, enabling the fine-tuning of vibrational characteristics through the incorporation of graphene reinforcements. The method allows for a comprehensive parametric evaluation, facilitating tailored vibration control. The analysis extends to symmetric and antisymmetric graphene distributions across the thickness, contributing to a thorough understanding of the material's behavior. However, certain limitations should be acknowledged. The exploration of parameters, including temperature gradients, taper forms, and various graphene types/shapes, is limited. The use of simplified interatomic potentials and interfacial behavior introduces constraints on the model's accuracy. Furthermore, the absence of stability/buckling analysis under thermal and mechanical loading, as well as the lack of transient dynamic analysis or comparison with experimental results, highlights areas for improvement. Lastly, manufacturing constraints related to multilayer graded microplates remain unaddressed, posing practical challenges to the implementation of the proposed method.

2. Mathematical formulation

As seen in Fig. 1, the present study concerns a multilayer rectangular FG-GPLRC microplate modeled as a laminated structure consisting of N_L discrete layers, each with identical thickness ($h_L(x,y) = \frac{h(x,y)}{N_L}$, the overall thickness is $h(x, y)$) and with dimensions L_x and L_y, which is placed on a viscoelastic foundation. In the current work, perfect bonding between the graphene-reinforced composite layers has been assumed for modeling simplicity and maintainability of analytical solutions. The viscoelastic foundation is defined by a damping coefficient c_d and Winkler stiffness k_w. The FG-GPLR microplate thickness is considered to vary linearly (Fig. 1a) or parabolically (Fig. 1b) along one or two directions, resulting in a non-uniform thickness profile. This study examines four distinct models of FG distribution to investigate the organization of the GPLs along the thickness direction (see Fig. 1c). The microplate is exposed to a thermal environment characterized by a temperature variation of ΔT. Different boundary conditions at the microplate's edges are taken into account. The following are two-dimensional thickness variations of the FG-GPLRC microplate, as well as examples of linear and parabolic thickness changes [49]:

$$h(x,y) = h_0\left(1 + \frac{\alpha x}{L_x} + \frac{\beta y}{L_y}\right), \text{ Bidirectional linear thickness variation,}$$
$$h(x,y) = h_0\left(1 + \frac{\alpha x^2}{L_x^2} + \frac{\beta y^2}{L_y^2}\right), \text{ Bidirectional parabolic thickness variation,} \quad (1)$$

In every scenario, h_0 represents the minimum thickness of the microplate. Furthermore, β and α present the taper parameters in y and x directions, respectively.

2.1. The material properties of the variable-thickness FG-GPLR microplate

The microplate is composed of a polymer matrix that is enhanced by the use of GPLs as filler material. The GPL reinforcements are graded in terms of both distribution and volume percentage along the thickness

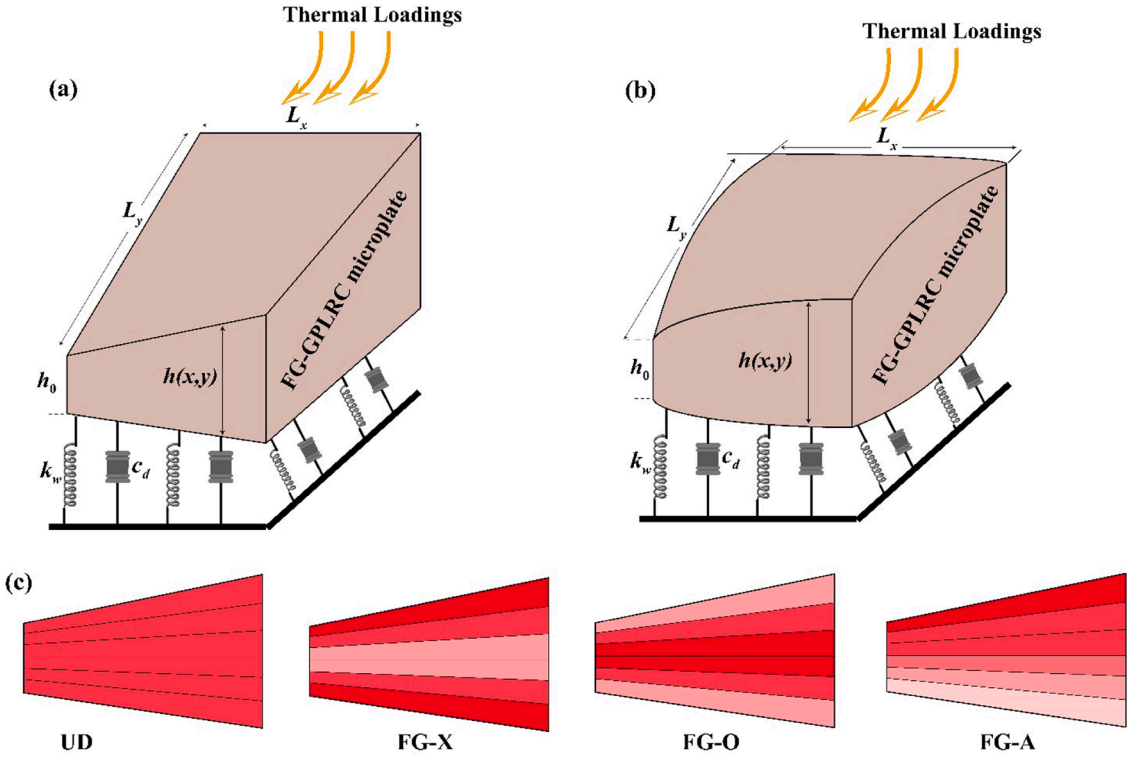

Fig. 1. A multilayer rectangular FG-GPLRC microplate of varying thickness resting on viscoelastic substrate as a function of temperature; (a) linearly varying thickness; (b) parabolically varying thickness; (c) four different FG models for the distribution of GPL reinforcements through the thickness.

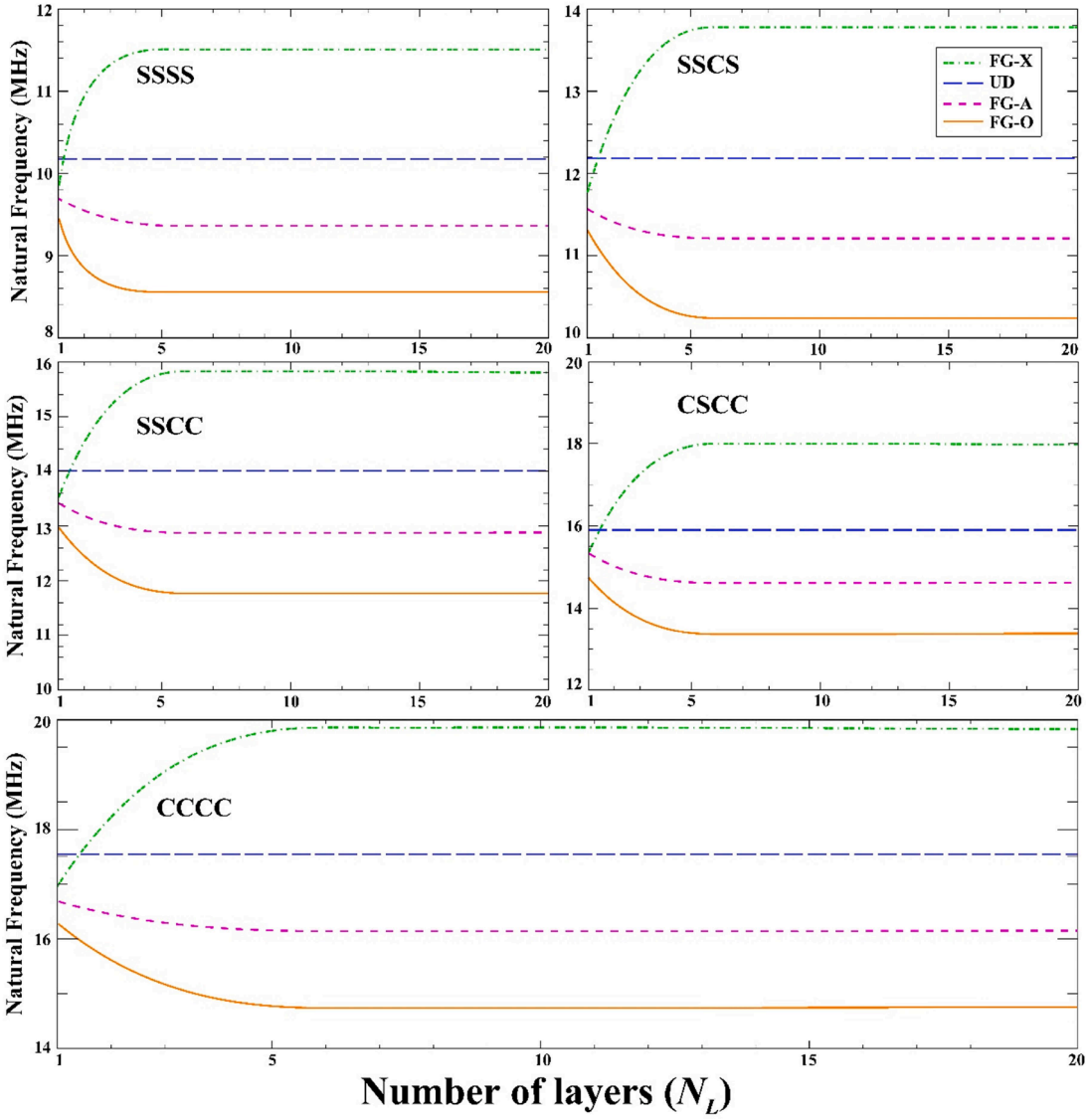

Fig. 2. Variation of the fundamental frequency of a linearly variable thickness FG-GPLRC microplate with number of layers for different GPL distributions and boundary conditions.

axis. The laminated microplate structure has separate layers, each characterized by a distinct weight percentage of GPLs. The following formula is used to get the weight fraction of GPLs in the kth layer [50], as seen in Fig. 2:

$$g_{GPL}^{(k)} = \begin{cases} g_{GPL}^{*}\ (\mathrm{UD}) \\ 4g_{GPL}^{*}\left[\dfrac{N_L+1}{2} - \left|k - \dfrac{N_L+1}{2}\right|\right]/(2+N_L),\ (\mathrm{FG-O}) \\ 4g_{GPL}^{*}\left[\dfrac{1}{2} - \left|k - \dfrac{N_L+1}{2}\right|\right]/(2+N_L),\ (\mathrm{FG-x}) \\ 2kg_{GPL}^{*}/(1+N_L),\ (\mathrm{FG-A}) \end{cases} \tag{2}$$

where $k = 1, 2, \ldots, N_L$. The term "g_{GPL}^{*}" denotes the mean value of the volume fraction of GPLs over the cross-sectional area of the microplate.

By changing the GPL gradation profile inside the laminated microstructure, both the static and dynamic responses may be optimized. The uniform distribution (UD) ensures that the weight fraction of GPLs is evenly distributed throughout all layers. In the FG-X model, the proportion of the GPL is seen to be highest at the upper and lower surfaces, exhibiting a steady decrease towards the intermediate layers. This provides superior strength and stiffness close to the borders. The FG-O pattern exhibits an inverse gradation, wherein the proportion of GPL is at its lowest on the surfaces and gradually increases towards the midplane in order to enhance the structural properties related to bending and shear. The FG-A pattern is designed to allocate the highest proportion of the GPL on the upper surface, gradually decreasing in a linear manner towards the lower surface. The attributes of each surface may be customized thanks to this asymmetric distribution. Using the weight fraction of GPLs (W_{GPL}), the density of the GPLs (ρ_{GPL}), and the

density of the polymer (ρ_M), one can simply calculate the volume fraction of GPLs (g^*_{GPL}) as [51]

$$V^{(k)}_{GPL} = \frac{W_{GPL}}{W_{GPL} + (\rho_{GPL}/\rho_M)(1 - W_{GPL})}, \tag{3}$$

The FG-laminate microplate, in contrast to a homogeneous composite, exhibits layer-wise variation in characteristics due to its spatially variable reinforcing distribution. The graded laminate is made up of separate layers, and each one has a different elastic modulus. This is because the percentage of graphene platelets in each layer varies. The computation of the effective Young's modulus ($E^{(k)}$) of the microplate is performed using the Halpin–Tsai model in the following manner [51]:

$$\begin{aligned} E^{(k)} &= \frac{3}{8}\frac{1+\zeta_L\eta_L g^{(k)}_{GPL}}{1-\eta_L g^{(k)}_{GPL}}E_M + \frac{5}{8}\frac{1+\zeta_w\eta_w g^{(k)}_{GPL}}{1-\eta_w g^{(k)}_{GPL}}E_M, \\ \eta_L &= \frac{\left(\frac{E_{GPL}}{E_M}\right)-1}{\left(\frac{E_{GPL}}{E_M}\right)+\zeta_L},\ \eta_w = \frac{\left(\frac{E_{GPL}}{E_M}\right)-1}{\left(\frac{E_{GPL}}{E_M}\right)+\zeta_w}, \end{aligned} \tag{4}$$

in which E_M and E_{GPL} represent the Young's modulus of the polymer matrix and Young's modulus of GPLs, respectively. Furthermore, the Halpin–Tsai equations for composite elastic moduli incorporate further factors (ζ_L,ζ_w) that are contingent upon the geometry and properties of the GNP reinforcements:

$$\zeta_L = 2\frac{a_{GPL}}{h_{GPL}},\ \zeta_w = 2\frac{b_{GPL}}{h_{GPL}}. \tag{5}$$

where a_{GPL},b_{GPL} and h_{GPL} represent the average dimensions of GPLs, specifically referring to their length, width, and thickness, respectively. The thermal expansion coefficient, denoted as $\alpha^{(k)}$, Poisson's ratio, denoted as $\vartheta^{(k)}$, and mass density, denoted as $\rho^{(k)}$, of the kth layer may be mathematically described using the rule of mixing.

$$\begin{aligned} \alpha^{(k)} &= \alpha_{GPL}V^{(k)}_{GPL} + \alpha_M\left(1 - V^{(k)}_{GPL}\right) \\ \vartheta^{(k)} &= \vartheta_{GPL}V^{(k)}_{GPL} + \vartheta_M\left(1 - V^{(k)}_{GPL}\right) \\ \rho^{(k)} &= \rho_{GPL}V^{(k)}_{GPL} + \rho_M\left(1 - V^{(k)}_{GPL}\right) \end{aligned} \tag{6}$$

where α_{GPL} and α_M refer to the thermal expansion of the GPLs and polymer matrix, respectively; ϑ_M and ϑ_{GPL} denote Poisson's ratios of the GPLs and polymer matrix, respectively.

2.2. MSGT

The MSGT is a sophisticated theoretical framework that enhances the traditional strain gradient theory, offering a more comprehensive understanding of material behavior at microscopic scales. Gradient tensors are of utmost importance in precisely characterizing the deformation and strain properties of materials, especially within micro- and nanostructural domains, in the context of the MSGT [11]. The strain energy ($\Xi_{\mathscr{V}}$) for a linear elastic continuum experiencing small deformations can be expressed in the following manner [11]:

$$\Xi_{\mathscr{V}} = 1/2\int_{\Omega}\left(\sigma_{ij}\varepsilon_{ij} + p_i\gamma_i + \tau^{(1)}_{ijk}\eta^{(1)}_{ijk} + m^s_{ij}\mathrm{X}^s_{ij}\right)dv, \tag{7}$$

where the dilatation gradient, deviatoric stretch gradient, strain, and symmetric rotation gradient tensors are characterized by γ_i, $\eta^{(1)}_{ijk}$, χ^s_{ij} and ε_{ij}, respectively. In addition, it is conventional to express the classical stress tensor as σ, whereas the higher-order stresses are denoted by p_i, $\tau^{(1)}_{ijk}$, and m^s_{ij} as

$$\begin{aligned} \sigma_{ij} &= \lambda^{(k)}\varepsilon_f\delta_{ij} + 2\mu^{(k)}\varepsilon_{ij} - \alpha^{(k)}\Delta T, \\ p_i &= 2\mu^{(k)}{l_0}^2\gamma_i, \\ \tau^{(1)}_{ijk} &= 2\mu^{(k)}{l_1}^2\mu\eta^{(1)}_{ijf}, \\ m^s_{ij} &= 2\mu^{(k)}{l_2}^2\mathrm{X}^s_{ij}, \end{aligned} \tag{8}$$

The symbol ΔT is used to denote the change in temperature or the difference between the reference temperature T_0 and the temperature at which the microplate was originally free from stress. The symbols $\mu^{(k)} = E^{(k)}/2(1 + \vartheta^{(k)})$ and $\lambda^{(k)} = E^{(k)}\vartheta^{(k)}/[(1 + \vartheta^{(k)})(1 - 2\vartheta^{(k)}]$ are used to represent the shear and bulk moduli, respectively. The symbol "l_0" denotes a fundamental length scale inherent to a material, which is closely associated with dilatation gradients and has a significant impact on its stiffness properties. The variable denoted as l_1 represents the characteristic length scale associated with deviatoric stretch gradients, which have an impact on both shear and extensional behavior. The symmetric rotation gradients linked to l_2 cause couple stresses. The inclusion of these three length parameters enables the independent assessment of the influences of dilatation, deviatoric, and rotational gradient effects on the mechanics of the microplate [52].

$$\varepsilon_{ij} = \frac{1}{2}\left(u_{i,j} + u_{j,i}\right), \tag{9}$$

$$\gamma_i = \varepsilon_{mm,i}, \tag{10}$$

$$\eta^{(1)}_{ijk} = \eta^{(1)}_{ijk} = \eta^s_{ijk} - \frac{1}{5}\left(\delta_{ij}\eta^s_{mmk} + \delta_{jk}\eta^s_{mmi} + \delta_{ki}\eta^s_{mmj}\right); \eta^s_{ijk} = \frac{1}{3}\left(\varepsilon_{jk,i} + \varepsilon_{ki,j} + \varepsilon_{ij,k}\right), \tag{11}$$

$$\mathrm{X}^s_{ij} = \frac{1}{2}\left(\theta_{i,j} + \theta_{j,i}\right); \theta_i = \frac{1}{2}(\mathrm{curl}(u))_i \tag{12}$$

The symbol " u " is used to represent the constituent parts of the displacement vector. In the context at hand, the symbol θ is applied to symbolize the infinitesimal rotation vector, whereas the symbol δ is utilized to designate the Kronecker delta.

2.3. Constitutive relations

The FSDT takes into account the effect of transverse shear flexibility by letting the normal direction stay linear, but not always perpendicular to the mid-surface after deformation. In the context of this study's theoretical framework, the conceptualization and modeling of the displacement field for each microplate are undertaken.

$$\begin{aligned} u_x(x,y,z,t) &= u_0(x,y,t) - z\psi_x(x,y,t), \\ u_y(x,y,z,t) &= v_0(x,y,t) - z\psi_y(x,y,t), \\ u_z(x,y,z,t) &= W_0(x,y,t), \end{aligned} \tag{13}$$

in which the microplate's middle plane rotates transversely around the y and x directions, which are shown by ψ_y and ψ_x, respectively. Furthermore, the z, y and x displacements of a point located at the center of the microplate's plane are denoted as W_0,v_0 and u_0, respectively. Employing the fundamental concepts of linear elasticity allows for the estimation of stresses inside a microplate. The following are some of the presumptions upon which this method is based:

Table 1
Validation of the plate's dimensionless fundamental natural frequency for various aspect ratios and taper parameters.

B.C	Taper parameter α	Aspect ratio	Ref. [58]	Present
SSSS	0.25	0.5	13.9359	13.9359
		1	22.3184	22.3184
		2	55.7438	55.7438
	0.5	0.5	15.6248	15.6248
		1	25.0742	25.0742
		2	62.4994	62.4993
	1	0.5	19.1764	19.1764
		1	30.9245	30.9245
		2	76.7057	76.7057
CCSS	0.25	0.5	21.3439	21.3436
		1	32.7193	32.7190
		2	84.2476	84.2475
	0.5	0.5	24.2965	24.2964
		1	37.2871	37.2870
		2	95.2379	95.2377
	1	0.5	30.3541	30.3538
		1	46.7716	46.7715
		2	118.3476	118.3475

$$\varepsilon_{xx} = \frac{\partial u_0}{\partial x} - z\frac{\partial \psi_x}{\partial x},$$
$$\varepsilon_{yy} = \frac{\partial v_0}{\partial y} - z\frac{\partial \psi_y}{\partial y},$$
$$\varepsilon_{xy} = \frac{1}{2}\left[\frac{\partial u_{0f}}{\partial y} + \frac{\partial v_0}{\partial x} - z\left(\frac{\partial \psi_x}{\partial y} + \frac{\partial \psi_y}{\partial x}\right)\right], \tag{14}$$
$$\varepsilon_{xz} = \frac{1}{2}\left(-\psi_x + \frac{\partial W_0}{\partial x}\right),$$
$$\varepsilon_{yz} = \frac{1}{2}\left(-\psi_y + \frac{\partial W_0}{\partial y}\right),$$

The normal strain components are denoted as ε_{xx},ε_{yy}, whereas the shear strain components are represented by ε_{xy},ε_{xz},ε_{yz}. The values of the non-zero components θ, X^s_{ij}, γ_i, and $\eta^{(1)}_{ijf}$ $(i,j,f = x,y,z)$ for the microplate may be derived by substituting Eqs. (13) and (14) into Eqs. (9–12), which can be found in Appendix A. The equations regulating the dynamic behavior of the FG-GPLR microplate, taking into account temperature and size dependence, are developed by applying Hamilton's principle [53].

$$\int_{t_0}^{t} (\delta\Xi_{\mathscr{T}} - \delta\Xi_{\mathscr{V}} + \delta\Xi_{\mathscr{W}})dt = 0. \tag{15}$$

Within this particular framework, the variable $\Xi_{\mathscr{W}}$ represents the conceptualization of the virtual work carried out by viscoelastic medium in conjunction with a temperature gradient. In the context being discussed, the variable $\Xi_{\mathscr{V}}$ represents the virtual strain energy, whereas $\Xi_{\mathscr{T}}$ is used to describe the virtual kinetic energy. The equation representing the change in kinetic energy may be expressed in the following manner:

$$\delta\Xi_{\mathscr{T}} = \int_V \rho^{(k)}\left[\dot{u}_x\delta\dot{u}_x + \dot{u}_y\delta\dot{u}_y + \dot{u}_z\delta\dot{u}_z\right]dV = \iint_A \left[\mathrm{I}_0\left(\frac{\partial u_0}{\partial t}\frac{\partial \delta u_0}{\partial t} + \frac{\partial v_0}{\partial t}\frac{\partial \delta v_0}{\partial t} + \frac{\partial W_0}{\partial t}\frac{\partial \delta W_0}{\partial t}\right)\right.$$
$$\left. + \mathrm{I}_1\left(\frac{\partial u_0}{\partial t}\frac{\partial \delta\psi_x}{\partial t} + \frac{\partial v_0}{\partial t}\frac{\partial \delta\psi_y}{\partial t} + \frac{\partial \psi_x}{\partial t}\frac{\partial \delta u_0}{\partial t} + \frac{\partial \psi_y}{\partial t}\frac{\partial \delta v_0}{\partial t}\right) + \mathrm{I}_2\left(\frac{\partial \psi_x}{\partial t}\frac{\partial \delta\psi_x}{\partial t} + \frac{\partial \psi_y}{\partial t}\frac{\partial \delta\psi_y}{\partial t}\right)\right]dA, \tag{16}$$

The variables V and A represent the volume and area of the cross-section, whereas the mass inertias are given in the following manner:

$$[I_0, I_1, I_2] = \int_{-h(x,y)/2}^{h(x,y)/2} \rho^{(k)}\left[1, z, z^2\right]dz, \tag{17}$$

Eqs. (8) and (14) can be inserted into Eq. (7) to express the variance in strain energy as follows:

$$\delta\Xi_{\mathscr{V}} = \int_v \left(\sigma_{xx}\delta\varepsilon_{xx} + \sigma_{yy}\delta\varepsilon_{yy} + \sigma_{xy}\delta\varepsilon_{xy} + \sigma_{yz}\delta\varepsilon_{yz} + \sigma_{xz}\delta\varepsilon_{xz} + p_x\delta\gamma_x\right.$$
$$p_y\delta\gamma_y + p_z\delta\gamma_z + \tau^{(1)}_{xxx}\delta\eta^{(1)}_{xxx} + \tau^{(1)}_{yyy}\delta\eta^{(1)}_{yyy} + \tau^{(1)}_{zzz}\delta\eta^{(1)}_{zzz} + \tau^{(1)}_{xxy}\delta\eta^{(1)}_{xxy} + \tau^{(1)}_{xyx}\delta\eta^{(1)}_{xyx}$$
$$+\tau^{(1)}_{yxx}\delta\eta^{(1)}_{yxx} + \tau^{(1)}_{xxz}\delta\eta^{(1)}_{xxz} + \tau^{(1)}_{xzx}\delta\eta^{(1)}_{xzx} + \tau^{(1)}_{zxx}\delta\eta^{(1)}_{zxx} + \tau^{(1)}_{yxx}\delta\eta^{(1)}_{yxx} + \tau^{(1)}_{yxy}\delta\eta^{(1)}_{yxy} + \tau^{(1)}_{xyy}\delta\eta^{(1)}_{xyy}$$
$$+\tau^{(1)}_{yyz}\delta\eta^{(1)}_{yyz} + \tau^{(1)}_{yzy}\delta\eta^{(1)}_{yzy} + \tau^{(1)}_{zyy}\delta\eta^{(1)}_{zyy} + \tau^{(1)}_{zzx}\delta\eta^{(1)}_{zzx} + \tau^{(1)}_{zxz}\delta\eta^{(1)}_{zxz} + \tau^{(1)}_{xzz}\delta\eta^{(1)}_{xzz} + \tau^{(1)}_{zzy}\delta\eta^{(1)}_{zzy}$$
$$+\tau^{(1)}_{zyz}\delta\eta^{(1)}_{zyz} + \tau^{(1)}_{yzz}\delta\eta^{(1)}_{yzz} + \tau^{(1)}_{xyz}\delta\eta^{(1)}_{xyz} + \tau^{(1)}_{yxz}\delta\eta^{(1)}_{yxz} + \tau^{(1)}_{zxy}\delta\eta^{(1)}_{zxy} + \tau^{(1)}_{zyx}\delta\eta^{(1)}_{zyx} + m^s_{xx}\delta X^s_{xx}$$
$$\left. + m^s_{yy}\delta X^s_{yy} + m^s_{zz}\delta X^s_{zz} + m^s_{xy}\delta X^s_{xy} + m^s_{xz}\delta X^s_{xz} + m^s_{yz}\delta X^s_{yz}\right)\mathrm{d}v. \tag{18}$$

The virtual work arising from the temperature environment and the viscoelastic medium may be characterized as follows [54]:

$$\delta\Xi_{\mathscr{W}} = \int_A \left[\left(k_w W_0 + c_d\frac{\partial W_0}{\partial t}\right)\delta W_0 + N^T_x\frac{\partial W_0}{\partial x}\delta\frac{\partial W_0}{\partial x} + N^T_y\frac{\partial W_0}{\partial y}\delta\frac{\partial W_0}{\partial y}\right]\mathrm{d}A,$$
$$N^T_x = N^T_y = N^T = \int_{-h(x,y)/2}^{h(x,y)/2} \frac{E^{(k)}}{1-\vartheta^{(k)}}\alpha^{(k)}T(z)dz,$$
$$T(z) = \left(\frac{1}{2} + \frac{z}{h(x,y)}\right)^{\varphi}\Delta T + T_0, \tag{19}$$

The parameter φ enables the representation of various thermal load profiles applied to the microplate. A uniform distribution, characterized by a value of φ equal to zero, indicates a consistent and unvarying rate of temperature change. The thermal stresses at the plate surfaces are more accurately represented by a linear profile with a value of φ equal to 1. Complex temperature fluctuations are made possible by nonlinear distributions (φ > 1), which capture nonlinear thermal effects on the

Table 2
Comparison of non-dimensional frequencies of a SSSS square microplate.

$\frac{L_x}{h_0}$	Mode	$\frac{l}{h_0}$	Present	Ref. [59]
5	1	0	0.2113	0.2113
		0.1	0.2263	0.2264
		0.2	0.2665	0.2666
		0.5	0.4563	0.4566
		1	0.8342	0.8344
	2	0	0.4622	0.4623
		0.1	0.4978	0.4978
		0.2	0.5904	0.5909
		0.5	1.0254	1.0255
		1	1.88561	1.8858
10	1	0	0.0577	0.0577
		0.1	0.0616	0.0617
		0.2	0.072	0.0725
		0.5	0.1226	0.124
		1	0.2264	0.2268
	2	0	0.1375	0.1376
		0.1	0.1474	0.1475
		0.2	0.1734	0.1736
		0.5	0.2976	0.2977
		1	0.5446	0.5448

microplate response [54]. By substituting Eqs. (16), (18), and (19) into Eq. (15), and considering the coefficients δu_0,δv_0,δW_0,$\delta\psi_x$ and $\delta\psi_y$ to be zero, the governing equations in the framework of the FSDT can be obtained as

$$\delta u_0: \frac{\partial N_{xx}}{\partial x}+\frac{\partial N_{xy}}{\partial y}+\frac{1}{2}\frac{\partial^2 Y_{xz}}{\partial xy}+\frac{1}{2}\frac{\partial^2 Y_{yz}}{\partial y^2}-\frac{\partial^2 P_x}{\partial x^2}-\frac{\partial^2 P_y}{\partial x\partial y}-\frac{\partial^2 T^{\tau}_{xxx}}{\partial x^2}-2\frac{\partial^2 T^{\tau}_{xxy}}{\partial x\partial y}-\frac{\partial^2 T^{\tau}_{yyx}}{\partial y^2}=$$
$$I_0\frac{\partial^2 u_0}{\partial t^2}+I_1\frac{\partial^2 \psi_x}{\partial t^2},$$
$$\delta v_0: \frac{\partial N_{xy}}{\partial x}+\frac{\partial N_{yy}}{\partial y}-\frac{1}{2}\frac{\partial^2 Y_{yz}}{\partial xy}-\frac{1}{2}\frac{\partial^2 Y_{xz}}{\partial x^2}-\frac{\partial^2 P_x}{\partial x\partial y}-\frac{\partial^2 P_y}{\partial y^2}-\frac{\partial^2 T^{\tau}_{xxy}}{\partial x^2}-2\frac{\partial^2 T^{\tau}_{yyx}}{\partial x\partial y}-\frac{\partial^2 T^{\tau}_{yyy}}{\partial y^2}=$$
$$I_0\frac{\partial^2 v_0}{\partial t^2}+I_1\frac{\partial^2 \psi_y}{\partial t^2},$$
$$\delta \mathrm{W}_0: \frac{\partial Q_x}{\partial x}+\frac{\partial Q_y}{\partial y}-\frac{1}{2}\frac{\partial^2 Y_{xx}}{\partial xy}+\frac{1}{2}\frac{\partial^2 Y_{yy}}{\partial xy}-\frac{1}{2}\frac{\partial^2 Y_{xy}}{\partial y^2}-\frac{\partial^2 T^{\tau}_{zzz}}{\partial x^2}-2\frac{\partial^2 T^{\tau}_{xyz}}{\partial x\partial y}-\frac{\partial^2 T^{\tau}_{yyz}}{\partial y^2}-k_w W_0-$$
$$c_d\frac{\partial W_0}{\partial t}+N^T\left(\frac{\partial^2 \mathrm{W}_0}{\partial x^2}+\frac{\partial^2 \mathrm{W}_0}{\partial y^2}\right)=I_0\frac{\partial^2 \mathrm{W}_0}{\partial t^2},$$
$$\delta\psi_x: \frac{\partial M_{xx}}{\partial x}+\frac{\partial M_{xy}}{\partial y}-Q_x+\frac{1}{2}\left(-\frac{\partial Y_{xy}}{\partial x}-\frac{\partial Y_{yy}}{\partial y}+\frac{\partial Y_{zz}}{\partial y}-\frac{\partial^2 H_{xz}}{\partial x\partial y}-\frac{\partial^2 H_{yz}}{\partial y^2}\right)+\frac{\partial^2 M^{\tau}_{xxx}}{\partial x^2}+$$
$$2\frac{\partial^2 M^{\tau}_{xxy}}{\partial x\partial y}+\frac{\partial^2 M^{\tau}_{yyx}}{\partial y^2}-2\frac{\partial T^{\tau}_{xyz}}{\partial y}-2\frac{\partial T^{\tau}_{zzz}}{\partial x}-\frac{\partial P_z}{\partial x}+\frac{\partial^2 M^{p}_{x}}{\partial x^2}+\frac{\partial^2 M^{p}_{y}}{\partial x\partial y}=I_1\frac{\partial^2 u_0}{\partial t^2}+I_2\frac{\partial^2 \psi_x}{\partial t^2}$$
$$\delta\psi_y: \frac{\partial M_{yyf}}{\partial y}+\frac{\partial M_{xy}}{\partial x}-Q_y+\frac{1}{2}\left(\frac{\partial Y_{xx}}{\partial x}-\frac{\partial Y_{zz}}{\partial x}+\frac{\partial Y_{xy}}{\partial y}+\frac{\partial^2 H_{xz}}{\partial x^2}+\frac{\partial^2 H_{yz}}{\partial x\partial y}\right)+\frac{\partial^2 M^{\tau}_{xxy}}{\partial x^2}+$$
$$2\frac{\partial^2 M^{\tau}_{yyx}}{\partial x\partial y}+\frac{\partial^2 M^{\tau}_{yyy}}{\partial y^2}-2\frac{\partial T^{\tau}_{xyz}}{\partial x}-2\frac{\partial T^{\tau}_{yyz}}{\partial y}-\frac{\partial P_z}{\partial y}+\frac{\partial^2 M^{p}_{x}}{\partial x\partial y}+\frac{\partial^2 M^{p}_{y}}{\partial y^2}=I_1\frac{\partial^2 v_0}{\partial t^2}+I_2\frac{\partial^2 \psi_y}{\partial t^2} \tag{20}$$

where

$$\left\langle N_{xx},N_{yy},N_{xy},Q_x,Q_y\right\rangle=\int_{-h(x,y)/2}^{h(x,y)/2}\left\langle \sigma_{xx},\sigma_{yy},\sigma_{xy},\kappa_s\sigma_{xz},\kappa_s\sigma_{yz}\right\rangle dz,$$
$$\left\langle M_{xx},M_{yy},M_{xy}\right\rangle=\int_{-h(x,y)/2}^{h(x,y)/2}\left\langle \sigma_{xx},\sigma_{yy},\sigma_{xy}\right\rangle z dz,$$
$$\left\langle Y_{xx},Y_{yy},Y_{zz},Y_{xy},Y_{xz},Y_{yz}\right\rangle=\int_{-h(x,y)/2}^{h(x,y)/2}\left\langle m^s_{xx},m^s_{yy},m^s_{zz},m^s_{xy},m^s_{xz},m^s_{yz}\right\rangle dz,$$
$$\left\langle H_{xz},H_{yz}\right\rangle=\int_{-h(x,y)/2}^{h(x,y)/2}\left\langle m^s_{xz},m^s_{yz}\right\rangle z dz,$$
$$\left\langle P_x,P_y,P_z\right\rangle=\int_{-h(x,y)/2}^{h(x,y)/2}\left\langle p_x,p_y,p_z\right\rangle dz,$$
$$\left\langle M^p_x,M^p_y\right\rangle=\int_{-h(x,y)/2}^{h(x,y)/2}\left\langle p_x,p_y\right\rangle z dz,$$
$$\left\langle M^{\tau}_{xxx},M^{\tau}_{yyy},M^{\tau}_{xxy},M^{\tau}_{yyx}\right\rangle=\int_{-h(x,y)/2}^{h(x,y)/2}\left\langle \tau^{(1)}_{xxx},\tau^{(1)}_{yyy},\tau^{(1)}_{xxy},\tau^{(1)}_{yyx}\right\rangle z dz,$$
$$\left\langle T^{\tau}_{xxx},T^{\tau}_{yyy},T^{\tau}_{zzz},T^{\tau}_{xxy},T^{\tau}_{xxz},T^{\tau}_{yyx},T^{\tau}_{yyz},T^{\tau}_{xyz}\right\rangle=\int_{-h(x,y)/2}^{h(x,y)/2}\left\langle \tau^{(1)}_{xxx},\tau^{(1)}_{yyy},\tau^{(1)}_{zzz},\tau^{(1)}_{xxy},\tau^{(1)}_{xxz},\tau^{(1)}_{yyx},\tau^{(1)}_{yyz},\tau^{(1)}_{xyz}\right\rangle dz \tag{21}$$

Table 3
Comparison of non-dimensional natural frequencies of an FG-GPLRC SSSS square plate for a variety of GPL distributions.

m, *n*	Study	Pure epoxy	UD	FG-O	FG-X	FG-A
1,1	Ref. [50]	0.0584	0.1216	0.102	0.1378	0.1118
	Ref. [60]	0.0584	0.1216	0.102	0.1378	0.1118
	Present	0.0584	0.1216	0.102	0.1378	0.1118
2,1	Ref. [50]	0.1391	0.2895	0.2456	0.3249	0.2673
	Ref. [60]	0.1391	0.2895	0.2456	0.3249	0.2673
	Present	0.1391	0.2895	0.2456	0.3249	0.2673
2,2	Ref. [50]	0.2132	0.4436	0.3796	0.4939	0.411
	Ref. [60]	0.2132	0.4436	0.3796	0.4939	0.411
	Present	0.2132	0.4436	0.3796	0.4939	0.411

In the given context, the symbol $\kappa_s = 5/6$ denotes the shear correction term and is based on the concept of shear correction to account for the variance of transverse shear strains across the thickness direction [55]. By integrating the parabolic shear strain distribution and equating the strain energy to that from conventional plate theory, a value of 5/6 enables modifying the constant transverse shear stiffness to better match solutions from elasticity theory. This is commonly used when dealing with rectangular cross-sections and has been validated in numerous studies for producing results that closely approximate three-dimensional elasticity solutions. The equilibrium equations for a microplate are derived and explained by inserting Eq. (21) into Eq. (20), taking into account Eqs. (8–12).

$$
\begin{aligned}
&\delta u_0:\ a_{11}\frac{\partial^2 u_0}{\partial x^2}+(a_{12}+a_{55})\frac{\partial^2 v_0}{\partial x\partial y}-b_{11}\frac{\partial^2 \psi_x}{\partial x^2}-(b_{12}+b_{55})\frac{\partial^2 \psi_y}{\partial x\partial y}-a_{55}\left[\left(2l_0^2+\frac{4}{5}l_1^2\right)\right.\\
&\left.\frac{\partial^4 u_0}{\partial x^4}-\frac{\partial^2 u_0}{\partial y^2}+\left(\frac{8}{15}l_1^2+\frac{1}{4}l_2^2\right)\ \frac{\partial^4 u_0}{\partial y^4}+\left(2l_0^2+\frac{4}{3}l_1^2+\frac{1}{4}l_2^2\right)\ \frac{\partial^4 u_0}{\partial x^2\partial y^2}\right]-a_{55}\left(2l_0^2+\frac{4}{15}l_1^2-\frac{1}{4}l_2^2\right)\\
&\left(\frac{\partial^4 v_0}{\partial x^3\partial y}+\frac{\partial^4 v_0}{\partial x\partial y^3}\right)+b_{55}\left[\left(2l_0^2+\frac{4}{5}l_1^2\right)\frac{\partial^4 \psi_x}{\partial x^4}-\frac{\partial^2 \psi_x}{\partial y^2}+\left(\frac{8}{15}l_1^2+\frac{1}{4}l_2^2\right)\ \frac{\partial^4 \psi_x}{\partial y^4}+\left(2l_0^2+\frac{4}{3}l_1^2+\frac{1}{4}l_2^2\right)\ \frac{\partial^4 \psi_x}{\partial x^2\partial y^2}\right]\\
&+b_{55}\left(2l_0^2+\frac{4}{15}l_1^2-\frac{1}{4}l_2^2\right)\left(\frac{\partial^4 \psi_y}{\partial x^3\partial y}+\frac{\partial^4 \psi_y}{\partial x\partial y^3}\right)=I_0\frac{\partial^2 u_0}{\partial t^2}+I_1\frac{\partial^2 \psi_x}{\partial t^2},\\
&\delta v_0:\ a_{11}\frac{\partial^2 v_0}{\partial y^2}+(a_{12}+a_{55})\frac{\partial^2 u_0}{\partial x\partial y}-b_{11}\frac{\partial^2 \psi_y}{\partial y^2}-(b_{12}+b_{55})\frac{\partial^2 \psi_x}{\partial x\partial y}+b_{55}\left(2l_0^2+\frac{4}{15}l_1^2-\frac{1}{4}l_2^2\right)\\
&\left(\frac{\partial^4 \psi_x}{\partial x^3\partial y}+\frac{\partial^4 \psi_x}{\partial x\partial y^3}\right)-a_{55}\left(2l_0^2+\frac{4}{15}l_1^2-\frac{1}{4}l_2^2\right)\left(\frac{\partial^4 u_0}{\partial x^3\partial y}+\frac{\partial^4 u_0}{\partial x\partial y^3}\right)+\\
&a_{55}\left[\frac{\partial^2 v_0}{\partial x^2}-\left(\frac{8}{15}l_1^2+\frac{1}{4}l_2^2\right)\ \frac{\partial^4 v_0}{\partial x^4}-\left(2l_0^2+\frac{4}{3}l_1^2+\frac{1}{4}l_2^2\right)\ \frac{\partial^4 v_0}{\partial x^2\partial y^2}-\left(2l_0^2+\frac{4}{5}l_1^2\right)\ \frac{\partial^4 v_0}{\partial y^4}\right]\\
&+b_{55}\left[-\frac{\partial^2 \psi_y}{\partial x^2}+\left(\frac{8}{15}l_1^2+\frac{1}{4}l_2^2\right)\ \frac{\partial^4 \psi_y}{\partial x^4}+\left(2l_0^2+\frac{4}{3}l_1^2+\frac{1}{4}l_2^2\right)\ \frac{\partial^4 \psi_y}{\partial x^2\partial y^2}+\left(2l_0^2+\frac{4}{5}l_1^2\right)\ \frac{\partial^4 \psi_y}{\partial y^4}\right]=I_0\frac{\partial^2 v_0}{\partial t^2}+I_1\frac{\partial^2 \psi_y}{\partial t^2}\\
&\delta \mathrm{W}_0:\ k_s a_{55}\left(\frac{\partial^2 W_0}{\partial x^2}+\frac{\partial^2 W_0}{\partial y^2}-\frac{\partial \psi_x}{\partial x}-\frac{\partial \psi_y}{\partial y}\right)-a_{55}\left(\frac{8}{15}l_1^2+\frac{1}{4}l_2^2\right)\left(\frac{\partial^4 W_0}{\partial x^4}+2\frac{\partial^4 W_0}{\partial x^2\partial y^2}+\frac{\partial^4 W_0}{\partial y^4}\right)+\\
&a_{55}\left(\frac{16}{15}l_1^2-\frac{1}{4}l_1^2\right)\left[\left(\frac{\partial^3 \psi_x}{\partial x^3}+\frac{\partial^3 \psi_x}{\partial x\partial y^2}\right)+\left(\frac{\partial^3 \psi_y}{\partial x^2\partial y}+\frac{\partial^3 \psi_y}{\partial y^3}\right)\right]\\
&-k_w W_0-c_d\frac{\partial W_0}{\partial t}+N^T\left(\frac{\partial^2 W_0}{\partial x^2}+\frac{\partial^2 W}{\partial y^2}\right)=I_0\left(\frac{\partial^2 W_0}{\partial t^2}\right),\\
&\delta \psi_x:\ k_s a_{55}\left(\frac{\partial \mathrm{W}_0}{\partial x}-\psi_x\right)-b_{11}\frac{\partial^2 u_0}{\partial x^2}-b_{55}\frac{\partial^2 u_0}{\partial y^2}-(b_{12}+b_{55})\frac{\partial^2 v_0}{\partial x\partial y}+b_{55}\left(2l_0^2+\frac{4}{15}l_1^2-\frac{1}{4}l_2^2\right)\\
&\left(\frac{\partial^4 v_0}{\partial x^3\partial y}+\frac{\partial^4 v_0}{\partial x\partial y^3}\right)-a_{55}\left(\frac{16}{15}l_1^2-\frac{1}{4}l_2^2\right)\left(\frac{\partial^3 W_0}{\partial x^3}+\frac{\partial^3 W_0}{\partial x\partial y^2}\right)-d_{55}\\
&\left[\left(2l_0^2+\frac{4}{5}l_1^2\right)\frac{\partial^4 \psi_x}{\partial x^4}+\left(2l_0^2+\frac{4}{3}l_1^2+\frac{1}{4}l_2^2\right)\ \frac{\partial^4 \psi_x}{\partial x^2\partial y^2}+\left(\frac{8}{15}l_1^2+\frac{1}{4}l_2^2\right)\ \frac{\partial^4 \psi_x}{\partial y^4}\right]\\
&+b_{55}\left[\left(2l_0^2+\frac{4}{5}l_1^2\right)\frac{\partial^4 u_0}{\partial x^4}+\left(2l_0^2+\frac{4}{3}l_1^2+\frac{1}{4}l_2^2\right)\ \frac{\partial^4 u_0}{\partial x^2\partial y^2}+\left(\frac{8}{15}l_1^2+\frac{1}{4}l_2^2\right)\ \frac{\partial^4 u_0}{\partial y^4}\right]+\\
&\left[a_{55}\left(2l_0^2+\frac{32}{15}l_1^2+\frac{1}{4}l_2^2\right)+d_{11}\right]\frac{\partial^2 \psi_x}{\partial x^2}+\left[d_{55}+a_{55}\left(\frac{4}{3}l_1^2+l_2^2\right)\right]\ \frac{\partial^2 \psi_x}{\partial y^2}+\left[a_{55}\left(2l_0^2+\frac{4}{5}l_1^2-\frac{3}{4}l_2^2\right)+d_{55}+d_{12}\right]\\
&\frac{\partial^2 \psi_y}{\partial x\partial y}-d_{55}\left(2l_0^2+\frac{4}{15}l_1^2-\frac{1}{4}l_2^2\right)\left(\frac{\partial^4 \psi_y}{\partial x^3\partial y}+\frac{\partial^4 \psi_y}{\partial x\partial y^3}\right)=I_1\frac{\partial^2 u_0}{\partial t^2}+I_2\frac{\partial^2 \psi_x}{\partial t^2}\\
&\delta \psi_y:\ k_s a_{55}\left(\frac{\partial \mathrm{W}_0}{\partial y}-\psi_y\right)-b_{11}\frac{\partial^2 v_0}{\partial y^2}-b_{55}\frac{\partial^2 v_0}{\partial x^2}-(b_{12}+b_{55})\frac{\partial^2 u_0}{\partial x\partial y}+b_{55}\left(2l_0^2+\frac{4}{15}l_1^2-\frac{1}{4}l_2^2\right)\\
&\left(\frac{\partial^4 u_0}{\partial x^3\partial y}+\frac{\partial^4 u_0}{\partial x\partial y^3}\right)-a_{55}\left(\frac{16}{15}l_1^2-\frac{1}{4}l_2^2\right)\left(\frac{\partial^3 W_0}{\partial x^2\partial y}+\frac{\partial^3 W_0}{\partial y^3}\right)-d_{55}\\
&\left[\left(\frac{8}{15}l_1^2+\frac{1}{4}l_2^2\right)\frac{\partial^4 \psi_y}{\partial x^4}+\left(2l_0^2+\frac{4}{3}l_1^2+\frac{1}{4}l_2^2\right)\ \frac{\partial^4 \psi_y}{\partial x^2\partial y^2}+\left(2l_0^2+\frac{4}{5}l_1^2\right)\ \frac{\partial^4 \psi_y}{\partial y^4}\right]\\
&+b_{55}\left[\left(\frac{8}{15}l_1^2+\frac{1}{4}l_2^2\right)\frac{\partial^4 v_0}{\partial x^4}+\left(2l_0^2+\frac{4}{3}l_1^2+\frac{1}{4}l_2^2\right)\ \frac{\partial^4 v_0}{\partial x^2\partial y^2}+\left(2l_0^2+\frac{4}{5}l_1^2\right)\ \frac{\partial^4 v_0}{\partial y^4}\right]+\\
&\left[a_{55}\left(2l_0^2+\frac{32}{15}l_1^2+\frac{1}{4}l_2^2\right)+d_{11}\right]\\
&\frac{\partial^2 \psi_y}{\partial y^2}+\left[d_{55}+a_{55}\left(\frac{4}{3}l_1^2+l_2^2\right)\right]\ \frac{\partial^2 \psi_y}{\partial x^2}+\left[a_{55}\left(2l_0^2+\frac{4}{5}l_1^2-\frac{3}{4}l_2^2\right)+d_{55}+d_{12}\right]\\
&\frac{\partial^2 \psi_x}{\partial x\partial y}-d_{55}\left(2l_0^2+\frac{4}{15}l_1^2-\frac{1}{4}l_2^2\right)\left(\frac{\partial^4 \psi_x}{\partial x^3\partial y}+\frac{\partial^4 \psi_x}{\partial x\partial y^3}\right)=I_1\frac{\partial^2 v_0}{\partial t^2}+I_2\frac{\partial^2 \psi_y}{\partial t^2}
\end{aligned}
\tag{22}
$$

where

$$\langle a_{11}, b_{11}, d_{11}\rangle = \int_{-h(x,y)/2}^{h(x,y)/2} \left[\lambda^{(k)} + 2\mu^{(k)}\right]\langle 1, z, z^2\rangle dz,$$
$$\langle a_{12}, b_{12}, d_{12}\rangle = \int_{-h(x,y)/2}^{h(x,y)/2} \lambda^{(k)}\langle 1, z, z^2\rangle dz, \tag{23}$$
$$\langle a_{55}, b_{55}, d_{55}\rangle = \int_{-h(x,y)/2}^{h(x,y)/2} \mu^{(k)}\langle 1, z, z^2\rangle dz,$$

3. The Galerkin procedure

The obtained size-dependent governing equations are solved by taking into account five possible combinations of simply supported and clamped boundary conditions for the FG-GPLRC microplate edges. The mathematical expression for the edge-clamped and simple-supported boundary conditions of the FG-GPLRC microplate is:

$$X_m(x) = \left[\sin\left(\frac{(n+0.25)\pi x}{L_x}\right) - \sinh\left(\frac{(n+0.25)\pi x}{L_x}\right)\right] - \left[\frac{\sin((n+0.25)\pi) + \sinh((n+0.25)\pi)}{\cos((n+0.25)\pi) + \cosh((n+0.25)\pi)}\right]\left[\cos\left(\frac{(n+0.25)\pi x}{L_x}\right) - \cosh\left(\frac{(n+0.25)\pi x}{L_x}\right)\right],$$
$$Y_n(y) = \left[\sin\left(\frac{(n+0.5)\pi y}{L_y}\right) - \sinh\left(\frac{(n+0.5)\pi y}{L_y}\right)\right] - \left[\frac{\sin((n+0.5)\pi) - \sinh((n+0.5)\pi)}{\cos((n+025)\pi) - \cosh((n+0.5)\pi)}\right]\left[\cos\left(\frac{(n+0.5)\pi y}{L_y}\right) - \cosh\left(\frac{(n+0.5)\pi y}{L_y}\right)\right] \tag{30}$$

For a clamped (*C*) edge:

$$u_0 = v_0 = W_0 = \psi_x = \psi_y = 0, \tag{24}$$

For a simply supported (*S*) edge:

$$\begin{aligned} v_0 = W_0 = \psi_y = N_{xx} = M_{xx} = 0, \ \text{at } x = 0, L_x, \\ u_0 = W_0 = \psi_x = N_{yy} = M_{yy} = 0, \ \text{at } y = 0, L_y, \end{aligned} \tag{25}$$

These boundary conditions must be met in addition to the governing equations for the solution to be acceptable. The following approximations are made to the microplate deflection in order to meet the simply supported boundary conditions [56]:

$$\langle u_0, \psi_x\rangle \sum_m^\infty \sum_n^\infty \frac{\partial X_m(x)}{\partial x} Y_n(y) \left\langle \breve{\mu}_0, \breve{\psi}_x \right\rangle e^{i\omega t},$$
$$\left\langle v_0, \psi_y\right\rangle \sum_m^\infty \sum_n^\infty \breve{V} X_m(x) \frac{\partial Y_n(y)}{\partial y} \left\langle \breve{v}_0, \breve{\psi}_y e^{i\omega t}\right\rangle, \tag{26}$$
$$W_0 = \sum_m^\infty \sum_n^\infty \breve{W} Y_n(y) X_m(x) e^{i\omega t},$$

where the unknown modal coefficients are denoted by the variables $\breve{u}_0$, $\breve{\psi}_x, \breve{v}_0, \breve{\psi}_y, \breve{W}_0$. Moreover, the variables m and n are representative of the half-wave numbers on the x and y axes, respectively. Additionally, the symbol ω denotes the natural frequency of the structure. It is important to acknowledge that the modal functions X_m and Y_n adhere to the boundary conditions and are stated in the following manner:

SSSS

$$X_m(x) = \sin\left(\frac{m\pi x}{L_x}\right), Y_n(y) = \sin\left(\frac{n\pi y}{L_y}\right) \tag{27}$$

SSCS

$$X_m(x) = \sin\left(\frac{m\pi x}{L_x}\right), Y_n(y) = \left[\sin\left(\frac{(n+0.25)\pi y}{L_y}\right) - \sinh\left(\frac{(n+0.25)\pi y}{L_y}\right)\right] - \left[\frac{\sin((n+0.25)\pi) + \sinh((n+0.25)\pi)}{\cos((n+0.25)\pi) + \cosh((n+0.25)\pi)}\right]\left[\cos\left(\frac{(n+0.25)\pi y}{L_y}\right) - \cosh\left(\frac{(n+0.25)\pi y}{L_y}\right)\right], \tag{28}$$

SSCC

$$X_m(x) = \sin\left(\frac{m\pi x}{L_x}\right), Y_n(y) = \left[\sin\left(\frac{(n+0.5)\pi y}{L_y}\right) - \sinh\left(\frac{(n+0.5)\pi y}{L_y}\right)\right] - \left[\frac{\sin((n+0.5)\pi) - \sinh((n+0.5)\pi)}{\cos((n+025)\pi) - \cosh((n+0.5)\pi)}\right]\left[\cos\left(\frac{(n+0.5)\pi y}{L_y}\right) - \cosh\left(\frac{(n+0.5)\pi y}{L_y}\right)\right], \tag{29}$$

CSCC

CCCC

$$X_m(x) = \left[\sin\left(\frac{(n+0.5)\pi x}{L_x}\right) - \sinh\left(\frac{(n+0.5)\pi x}{L_x}\right)\right] - \left[\frac{\sin((n+0.5)\pi) - \sinh((n+0.5)\pi)}{\cos((n+0.5)\pi) - \cosh((n+0.5)\pi)}\right]\left[\cos\left(\frac{(n+0.5)\pi x}{L_x}\right) - \cosh\left(\frac{(n+0.5)\pi x}{L_x}\right)\right]$$
$$Y_n(y) = \left[\sin\left(\frac{(n+0.5)\pi y}{L_y}\right) - \sinh\left(\frac{(n+0.5)\pi y}{L_y}\right)\right] - \left[\frac{\sin((n+0.5)\pi) - \sinh((n+0.5)\pi)}{\cos((n+025)\pi) - \cosh((n+0.5)\pi)}\right]\left[\cos\left(\frac{(n+0.5)\pi y}{L_y}\right) - \cosh\left(\frac{(n+0.5)\pi y}{L_y}\right)\right] \tag{31}$$

The Galerkin method will be employed in order to obtain a set of algebraic equations that represent the governing equations. The process involves replacing the presumed deflection expressions (Eq. (26)) within the partial differential equations that describe the motion (Eq. (22)). The orthogonality between the residual and the test function systems may be demonstrated as follows:

$$\iint R(x, y) X_m(x) Y_n(y) dx dy = 0, \ m, n = 1, 2, 3, \ldots \tag{32}$$

The representation of equilibrium equations can be achieved through the utilization of a matrix, employing the formula provided in connection (32).

$$\left([M]_{5\times5}\omega^2 - [K]_{5\times5}\right)\bar{q} = 0 \tag{33}$$

where $[K]_{5\times5}$ and $[M]_{5\times5}$ represent the stiffness and mass characteristics, respectively, and $\bar{\mathbf{q}} = (\breve{u}_0, \breve{\psi}_x, \breve{v}_0, \breve{\psi}_y, \breve{W}_0)^T$. In order to calculate the natural frequencies, it is necessary to find a non-trivial solution to the characteristic Eq. (33). The aforementioned objective is accomplished by equating the determinant of the coefficient matrix on the left-

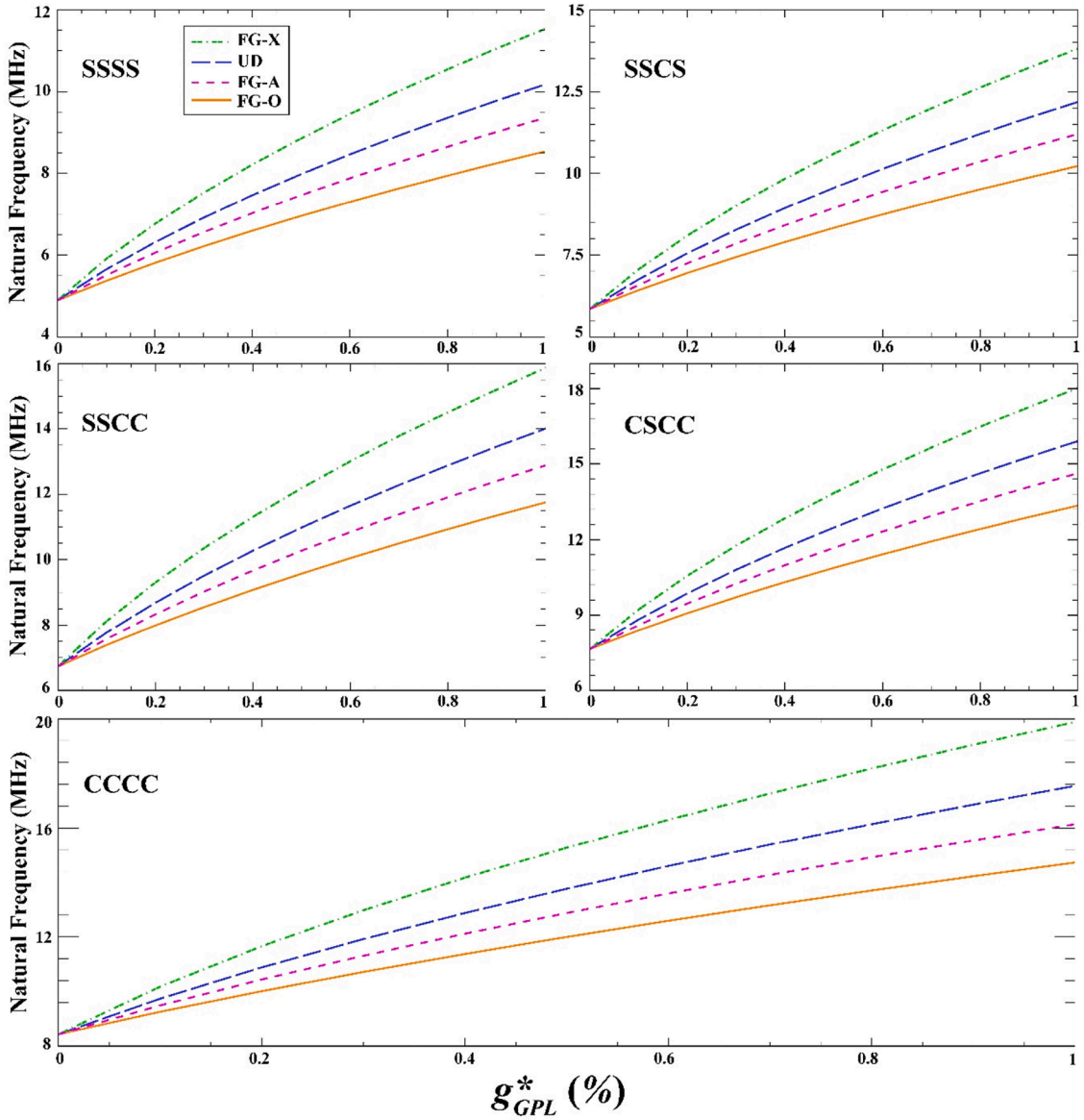

Fig. 3. Influence of weight fraction on the vibrations of a linearly variable-thickness FG-GPLRC microplate.

hand side of Eq. (33) to zero.

4. Findings and discussion

According to earlier research, a laminated microplate with PLRC that have at least 10 ($N_L = 10$) distinct layers can be a good representation of an FG microplate continuum. As the quantity of laminae reinforced with the GPL rises, the gradual transition of material properties takes on a more continuous and smoother pattern, approaching the characteristics of an ideal FGM [57]. The dimensions of GPLs are as follows: $a_{GPL} = 2.5\mu m$, $b_{GPL} = 1.5\mu m$, and $h_{GPL} = 1.5nm$. The epoxy polymer matrix and GPLs are thought to display temperature-dependent mechanical properties, which are described as [57]

$E_M = (4854.5 - 6.1816T)\text{MPa},\ \vartheta_M = 0.34,\ \rho_M = 1200\text{kg}/\text{m}^3,\ \ \alpha_M = 60 \times 10^{-6}(1/K),$
$E_{GPL} = (1087.8 - 0.261T)\text{GPa},\ \vartheta_{GPL} = 0.186,\ \rho_{GPL} = 1062.5\text{kg}/\text{m}^3,\ \alpha_{GPL} = (13.92 - 0.0299T) \times 10^{-6}(1/K),$

The specific values of length scale parameters used in the analysis are chosen considering the typical ranges reported in the literature related to gradient elasticity theories. These length scales have so far been predominantly quantified through calibration procedures based on molecular dynamics simulations of structures at the micro/nanolevel under varied loading conditions.

4.1. Validation of the model structure

During model validation, the validity and trustworthiness of the suggested procedure are extensively tested. In the first validation, using the current model and not taking into account temperature, viscoelastic medium, and GPL effects, Table 1 shows the first natural frequency ($\varpi =$

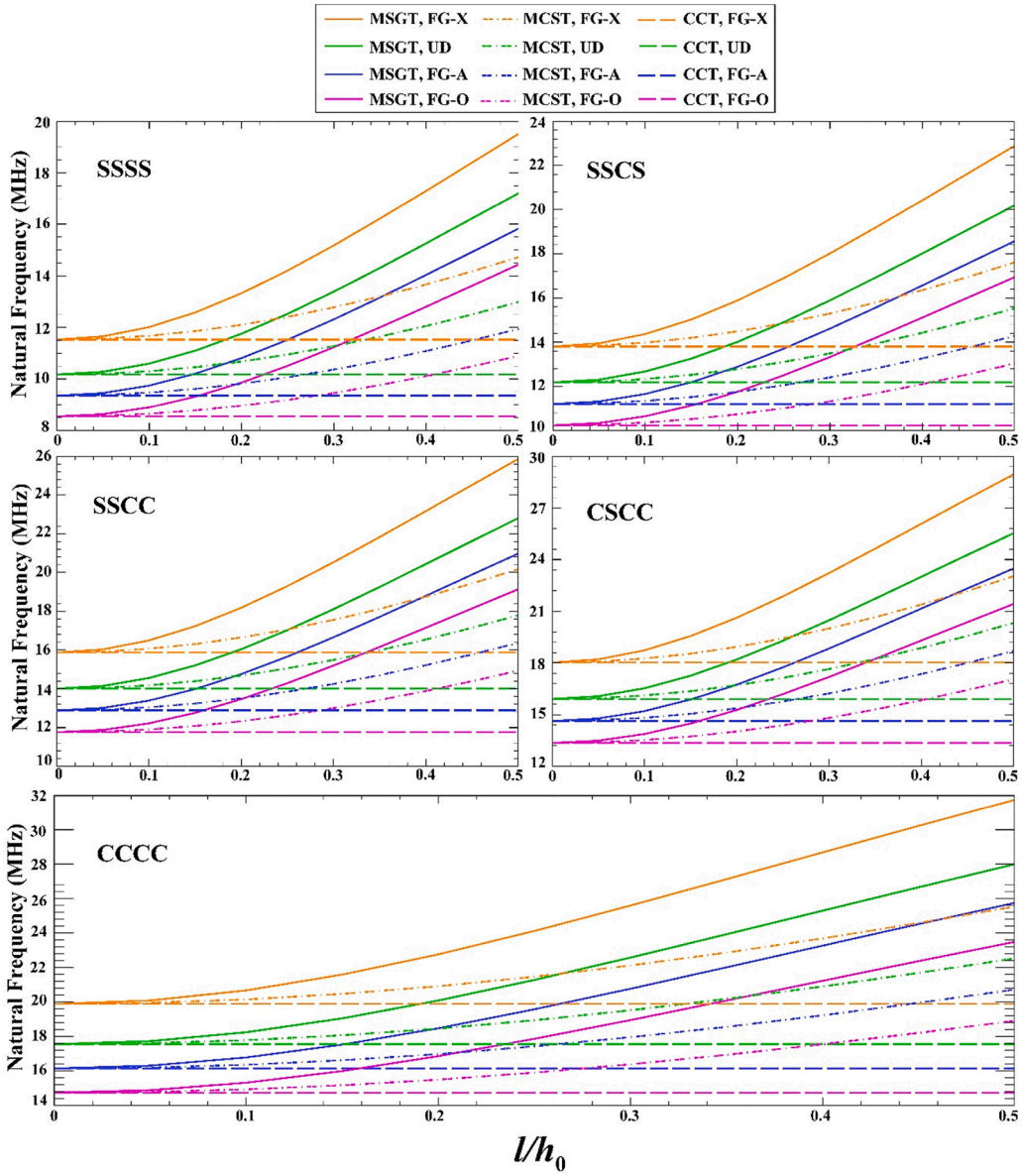

Fig. 4. Effects of length scale parameter and GPL distributions on natural frequency changes of a linearly variable thickness FG-GPLRC microplate for different theories.

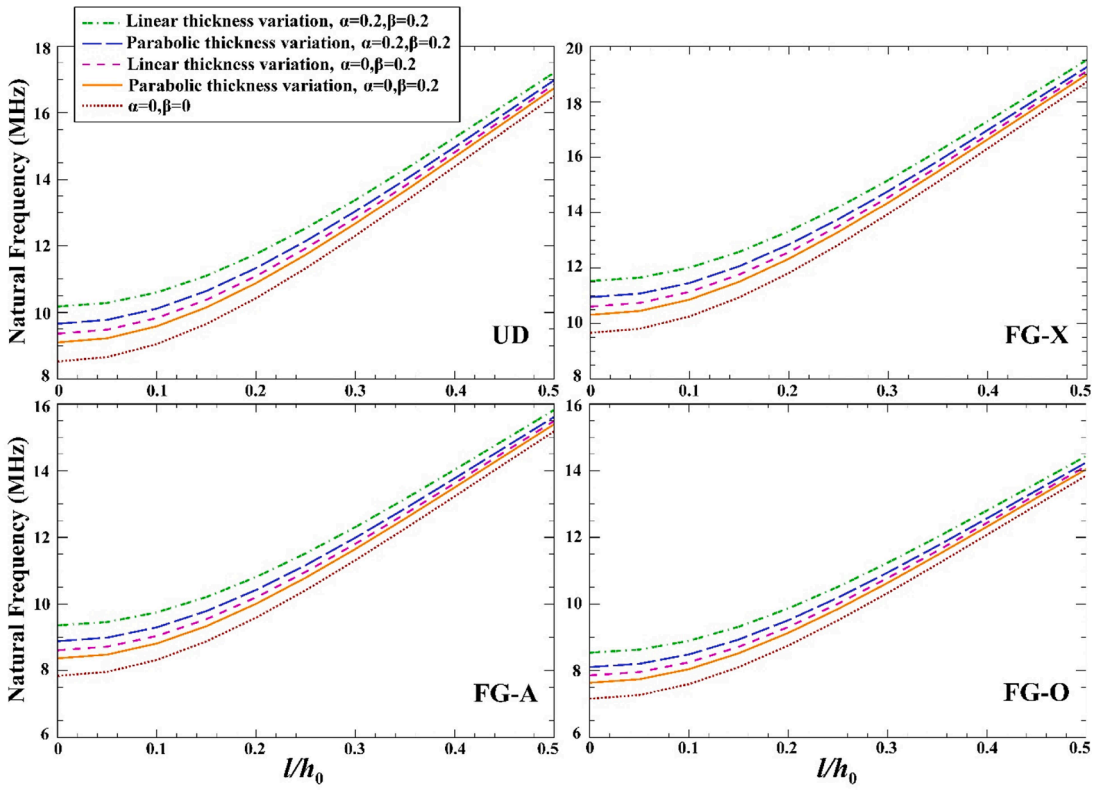

Fig. 5. The effects of linearly and parabolically changing thickness models on the change of the FG-GPLRC microplate's first natural frequency.

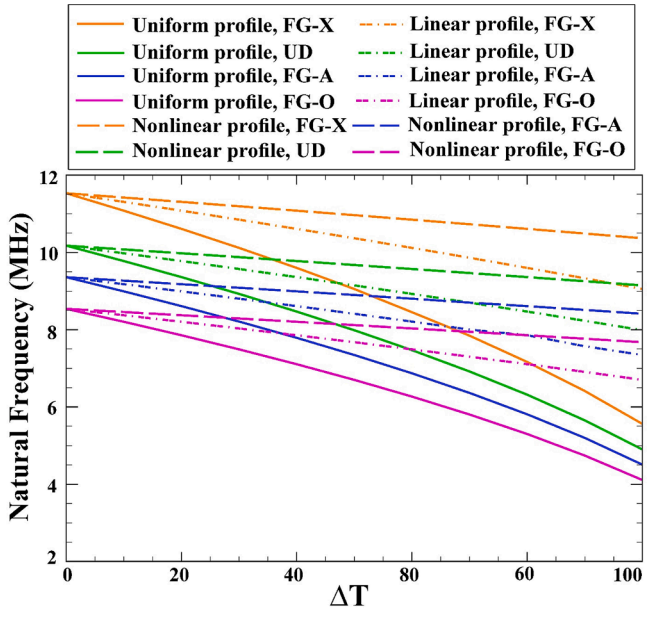

Fig. 6. Effects of the temperature and different temperature profiles on the natural frequency of a SSSS FG-GPLRC microplate.

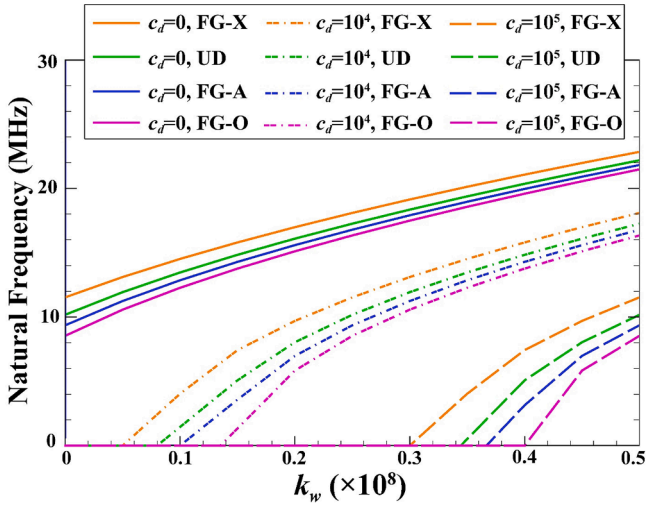

Fig. 7. Effects of viscoelastic medium damping coefficient and Winkler stiffness on the natural frequency of a SSSS FG-GPLRC microplate.

$\omega L_x{}^2\sqrt{\rho h_0/d_{11}}$) of an isotropic plate whose thickness changes linearly in one direction for two different boundary conditions. The data are acquired for various aspect ratios and taper parameters. The findings are compared to the results presented in Ref. [58], which employed classical laminated plate theory. The comparison demonstrates a strong concurrence between the findings presented in this study and the analytical predictions outlined in Ref. [58].

In the subsequent validation process, the non-dimensional frequencies $\varpi = \omega h_0\sqrt{\rho_M/E_M}$ of a square SSSS microplate with uniform thickness are determined for various mode numbers and dimensionless length scale parameters (l/h_0,$l = l_0 = l_1 = l_2$), while disregarding the influence of GPL, viscoelastic media, and thermal effects. The outcomes are compared with Ref. [59] in Table 2 in terms of the strain gradient parameter. The successful validation of the proposed methodology against the analytical data provided in Reference [59] demonstrates its efficacy and accuracy in forecasting the dimensionless natural frequency.

The final validation of the present model involves obtaining the dimensionless natural frequencies $\varpi = \omega h_0\sqrt{\rho_M/E_M}$ of an FG-GPLRC SSSS square plate with uniform thickness ($L_x/h_0 = 10$) for a variety of

GPL distributions. This is done without taking into account the presence of a viscoelastic medium, temperature effects, and MSGT. The obtained results are compared with the findings presented in Refs. [50,60], as shown in Table 3. The analysis suggests that the proposed methodology has remarkable effectiveness, surpassing the outcomes reported in the previously stated literature. It is noted that all distributions of the FG-GPLRC plate have a higher natural frequency than the pure epoxy plate. GPLs exhibit a significantly higher Young's modulus, measuring over 1000 GPa, in comparison to epoxy materials, which typically possess a Young's modulus of approximately 3 GPa.

4.2. Parametric study

Fig. 2 examines, for a variety of GPL distributions, how the number of layers and the boundary conditions affect the natural frequency of a linearly variable-thickness FG-GPLRC microplate when $L_x = L_y = 20\ \mu$m, $h_0 = 1.76\ \mu$m, $g^*_{GPL} = 1$ %, $m = 1$, $n = 1$, $\alpha = 0.2$, $\beta = 0.2$, $\Delta T = 0$, $l_0 = l_1 = l_2 = 0$, $k_w = 0$, $c_d = 0$. Since the UD distribution has a homogenous design, as would be predicted, the fundamental frequencies remain constant despite the number of layers changing. In the case of FG-O and FG-A distributions, the first decline in natural frequency is observed as the number of GPL layers increases. However, after the number of layers reaches a range of 5–10, the natural frequency stabilizes and remains constant. In contrast, the FG-X distribution exhibits an initial increase in frequency as the number of layers increases, followed by a stabilization phase. The initial decrease in frequency for FG-O and FG-A arrangements is attributed to the additional interlayer shear flexibility introduced by higher layering, which lowers overall stiffness. In the FG-X design, the introduction of additional layers enriched with GPL in close proximity to the surfaces yields a notable enhancement in bending stiffness, resulting in an increase in frequency. The ensuing stabilization occurs when the dominance of shear flexibility counteracts any additional stiffness advantages gained from additional layers. The findings of the study also demonstrate that the FG-X distribution produces the highest natural frequency, while the FG-O distribution results in the lowest frequency. The increased bending stiffness of the FG-X design is a result of the greater reinforcing of the GPL at the surfaces. The FG-O distribution exhibits a tendency to concentrate reinforcements internally, resulting in an improvement in shear stiffness. Furthermore, the natural frequency was lowest for SSSS conditions with the least restriction and highest for CCCC boundary conditions, which offer the maximum edge restraint. The following is the frequency ordering based on boundary conditions: CCCC > CSCC > SSCC > SSCS > SSSS.

Fig. 3 displays the influence of weight fraction on the vibrations of a linearly variable-thickness FG-GPLRC microplate under various boundary conditions for a variety of patterns (including a FG-O, UD, FG-X, and FG-A pattern) when $L_x = L_y = 20\mu$m, $h_0 = 1.76\mu$m, $N_L = 10$, $m = 1$, $n = 1$, $\alpha = 0.2$, $\beta = 0.2$, $\Delta T = 0$, $l_0 = l_1 = l_2 = 0$, $k_w = 0$, $c_d = 0$. Results show that all FG-O, UD, FG-X, and FG-A arrangements have no discernible effect on the natural frequency when the weight percentage of GPLs is zero. As the weight fraction of the GPL increases, the distinctions in vibration characteristics across the distributions become increasingly evident. The natural frequency of the system experiences a substantial increase as the weight fraction of GPL reinforcements increases. The significant enhancement in bending stiffness can be attributable to the presence of graphene platelets. An increase in the weight fractions of higher GPLs leads to an elevation in the Young's modulus and an enhancement of the second moment of area. Consequently, this results in a significant rise in stiffness and natural frequency. The FG-X distribution exhibits the maximum frequency, while the FG-O arrangement shows the lowest frequency. The FG-X configuration has more GPLs near the surfaces, improving bending response. The FG-O distribution concentrates reinforcements internally, enhancing shear characteristics.

The study presented in Fig. 4 examines the effect of various factors, namely the dimensionless length scale parameter (l/h, $l = l_0 = l_1 = l_2$), GPL distributions, and different boundary conditions, on the changes in the natural frequency of a linearly variable-thickness FG-GPLRC microplate. The investigation encompasses three different theories: the CCT, where $l_0 = l_1 = l_2 = 0$; the MCST, where $l_0 = l_1 = 0$, $l_2 \neq 0$; and the MSGT, where $l_0 = l_1 = l_2 \neq 0$. For this case, let's assume that $L_x = L_y = 20\ \mu$m, $h_0 = 1.76\ \mu$m, $N_L = 10$, $m = 1$, $n = 1$, $\alpha = 0.2$, $\beta = 0.2$, $\Delta T = 0$, $g^*_{GPL} = 1$ %, $k_w = 0$, $c_d = 0$. The results suggest that the frequency changes for the CCT stay consistent regardless of the values of the length scale parameter, as this parameter does not affect the CCT. The length scale parameter is utilized to quantify the influence of size effects that are observable at microscales. An augmentation in the magnitude of this parameter gives rise to a concomitant escalation in strain energy, resulting in heightened rigidity and natural frequency. As previously demonstrated, an increase in this particular parameter leads to heightened rigidity and natural frequency as a consequence of an augmented strain energy density. Adding rotation gradients to the MSGT also makes it stiffer compared to just adding couple stresses to the MCST.

The effects of linearly and parabolically changing thickness models on the change of the FG-GPLRC microplate's first natural frequency are shown in Fig. 5 when $L_x = L_y = 20\ \mu$m, $h_0 = 1.76\ \mu$m, $N_L = 10$, $m = 1$, $n = 1$, $g^*_{GPL} = 1$ %, $\Delta T = 0$, $l_0 = l_1 = l_2 = 0$, $k_w = 0$, $c_d = 0$. This analysis is conducted under various boundary conditions and distributions of GPL. An increase in the natural frequency is observed when the thickness profile parameters α and β are increased, regardless of whether the thickness fluctuations follow a linear or parabolic pattern. The observed phenomenon can be related to the general trend of increased stiffness as the thickness of the microplate increased in both the length and width dimensions, characterized by greater values of α and β. The presence of a parabolic thickness variation results in a more significant decrease in frequency as compared to a linear profile. The increased flexibility towards the edges is a result of the parabolic taper, which leads to accelerated thinning. For a given α and β, the linear thickness variation provides higher stiffness and natural frequency than the parabolic case, owing to its more gradual thickness reduction. At $\alpha = \beta = 0$, both models approach a microplate of constant thickness, exhibiting the same frequency. As the values of the taper parameters grow larger, the natural frequencies will diverge more and more due to the differences in flexural rigidity between the linear and parabolic situations.

Fig. 6 shows how temperature and different temperature profiles change the natural frequency of an FG-GPLRC microplate with a linearly variable thickness under the SSSS boundary conditions when $L_x = L_y = 20\ \mu$m, $h_0 = 1.76\ \mu$m, $N_L = 10$, $m = 1$, $n = 1$, $\alpha = 0.2$, $\beta = 0.2$, $g^*_{GPL} = 1$ %, $l_0 = l_1 = l_2 = 0$, $k_w = 0$, $c_d = 0$. The thermal distribution patterns considered in this study include the uniform ($\varphi = 0$), linear ($\varphi = 1$), and nonlinear ($\varphi = 3$) distributions. The findings indicate that, irrespective of the temperature profile, a rise in temperature change leads to a decrease in frequency. However, the frequency drop is most pronounced for a uniform temperature distribution compared to linear and nonlinear profiles. Furthermore, the nonlinear temperature profile induces the smallest frequency shift with temperature. As the temperature rises, the disparities in frequency response between the temperature profiles become increasingly pronounced. This phenomenon can be linked to the uniformity of temperature, which leads to consistent thermal expansion and a decrease in stiffness across the whole thickness of the microplate. In contrast, in the case of nonlinear profiles, regions characterized by lower temperatures exhibit a diminished degree of thermal softening,

hence mitigating the influence on the overall stiffness. It is also observed that the differences in frequency response between the GPL distribution models decrease with rising temperature. At higher temperatures, the large uniform thermal strains dominate over the reinforcing effects of GPL gradients.

Lastly, Fig. 7 presents the effects of viscoelastic medium damping coefficient and Winkler stiffness for simply supported boundary conditions on the natural frequency of a FG-GPLRC microplate with linearly variable thickness when $L_x = L_y = 20\ \mu$m, $h_0 = 1.76\ \mu$m, $N_L = 10$, $m = 1$, $n = 1$, $\alpha = 0.2$, $\beta = 0.2$, $g^*_{GPL} = 1\ \%$, $l_0 = l_1 = l_2 = 0, \Delta T = 0$. The natural frequency is shown to increase as the Winkler stiffness kw is increased for a certain c_d. The increased overall stiffness and frequency of the system are a result of the stronger elastic foundation providing greater resistance to plate deflection. On the other hand, when considering a specific value of k_w, augmenting the damping coefficient cd results in a decrease in the natural frequency. Increased damping results in a reduction in vibration amplitude and dynamic responsiveness, leading to a decrease in frequency.

5. Conclusions

This study presented a comprehensive analytical investigation into the vibration characteristics of FG-GPLRC microplates with linearly and parabolically tailored thickness profiles resting on viscoelastic medium under thermal loading and various boundary conditions. The implementation of the Halpin–Tsai model was employed in order to determine the effective material properties pertaining to various distributions of GPLs. Size effects were taken into consideration by the governing equations, which were based on MSGT and FSDT. An efficient Galerkin method solved the final governing equations. The results demonstrated the significant influences of the length scale parameter, temperature change, boundary conditions, GPL distribution pattern, thickness profile, GPL weight fraction, temperature distribution profiles, and viscoelastic medium on the natural frequencies of the FG-GPLRC microplates. The extensive dataset presented can be utilized to enhance the design optimization of variable-thickness FG-GPLRC microplates for applications in MEMS. The study demonstrates the potential for extensive tuning of dynamics through careful tailoring of gradation profiles and arrangements. Key findings that emerged from this research include:

- The thickness gradation profile had a pronounced influence on the vibration behavior. Parabolic thickness variations induced greater flexibility and lower frequency compared to linear variations. The vibration frequency increased with higher values of the thickness taper constants.
- A rise in temperature change leads to a decrease in frequency. However, the frequency drop is most pronounced for a uniform temperature distribution compared to linear and nonlinear profiles. Furthermore, the nonlinear temperature profile induces the smallest frequency shift with temperature
- The FG-X arrangement with more graphene near surfaces provided highest stiffness and frequency, while FG-O distribution with internal gradation offered lowest frequency.
- Increasing GPL weight fraction drastically improved frequency due to enhancement of bending rigidity.

Institutional review board statement

Not applicable.

Informed consent statement

Not applicable.

Funding

This research received no external funding.

CRediT authorship contribution statement

Jintara Lawongkerd: Writing – review & editing, Writing – original draft, Validation, Supervision, Software, Project administration, Investigation, Funding acquisition, Formal analysis, Data curation, Conceptualization. **Peyman Roodgar Saffari:** Writing – review & editing, Writing – original draft, Visualization, Validation, Supervision, Software, Project administration, Methodology, Investigation, Funding acquisition, Formal analysis, Data curation, Conceptualization. **Thira Jearsiripongkul:** Validation, Software, Resources, Project administration, Methodology, Investigation, Formal analysis, Conceptualization. **Chanachai Thongchom:** Writing – review & editing, Visualization, Validation, Supervision, Project administration, Investigation, Formal analysis, Data curation, Conceptualization. **Sikiru Oluwarotimi Ismail:** Writing – review & editing, Validation, Resources, Project administration, Investigation, Funding acquisition, Formal analysis, Conceptualization. **Pouyan Roodgar Saffari:** Writing – review & editing, Writing – original draft, Software, Methodology, Investigation, Funding acquisition, Formal analysis, Data curation, Conceptualization. **Suraparb Keawsawasvong:** Writing – original draft, Visualization, Software, Resources, Methodology, Investigation, Data curation, Conceptualization.

Declaration of competing interest

The authors declare that they have no known competing financial interests or personal relationships that could have appeared to influence the work reported in this paper.

Data availability

Data will be made available on request.

Acknowledgments

This study was supported by Thammasat Postdoctoral Fellowship, Thammasat University Research Division, Thammasat University.

Appendix A

The non-zero components θ, X^s_{ij}, γ_i and $\eta^{(1)}_{ijf}$ $(i,j,f = x,y,z)$ for each FG microplate can be presented as:

$$\theta_x = -\frac{1}{2}\left(W_{0,y} + \psi_y\right),$$

$$\theta_y = -\frac{1}{2}\left(W_{0,x} + \psi_x\right),$$

$$\theta_z = \frac{1}{2}\left(v_{0,x} - z\psi_{y,x} - u_{0,y} + z\psi_{x,y}\right),$$

$$\mathrm{X}^s_{xx} = \frac{1}{2}\left(W_{0,xy} + \psi_{y,x}\right),$$

$$\mathrm{X}^s_{yy} = -\frac{1}{2}\left(W_{0,xy} + \psi_{x,y}\right),$$

$$\mathrm{X}^s_{zz} = \frac{1}{2}\left(\psi_{x,y} - \psi_{y,x}\right),$$

$$\mathrm{X}^s_{xy} = \frac{1}{4}\left(W_{0,yy} + \psi_{y,y} - W_{0,xx} - \psi_{x,x}\right),$$

$$\mathrm{X}^s_{xz} = \frac{1}{4}\left(v_{0,xx} - z\psi_{y,xx} - u_{0,xy} + z\psi_{x,xy}\right),$$

$$\mathrm{X}^s_{yz} = \frac{1}{4}\left(v_{0,xy} - z\psi_{y,xy} - u_{0,yy} + z\psi_{x,yy}\right),$$

$$\gamma_x = u_{0,xx} - z\psi_{x,xx} + v_{0,xy} - z\psi_{y,xy},$$

$$\gamma_y = v_{0,yy} - z\psi_{y,yy} + u_{0,xy} - z\psi_{x,xy},$$

$$\gamma_z = -\left(\psi_{x,x} + \psi_{y,y}\right), \tag{A}$$

$$\eta^{(1)}_{xxx} = \frac{1}{5}\left(2u_{0,xx} - u_{0,yy} - 2v_{0,xy} - 2z\psi_{x,xx} + z\psi_{x,yy} + 2z\psi_{y,xy}\right),$$

$$\eta^{(1)}_{yyy} = \frac{1}{5}\left(2v_{0,yy} - v_{0,xx} - 2u_{0,xy} - 2z\psi_{y,yy} + z\psi_{y,xx} + 2z\psi_{x,xy}\right),$$

$$\eta^{(1)}_{zzz} = \frac{2}{5}\left(\psi_{x,x} + \psi_{y,y}\right) - \frac{1}{5}\left(W_{0,xx} + W_{0,yy}\right),$$

$$\eta^{(1)}_{xxy} = \eta^{(1)}_{xyx} = \eta^{(1)}_{yxx} = \frac{1}{15}\left(4v_{0,xx} + 8u_{0,xy} - 3v_{0,yy}\right) - \frac{1}{15}z\left(8\psi_{x,xy} + 4\psi_{y,xx} - 3\psi_{y,yy}\right),$$

$$\eta^{(1)}_{xxz} = \eta^{(1)}_{xzx} = \eta^{(1)}_{zxx} = \frac{1}{15}\left(4W_{0,xx} - W_{0,yy} - 8\psi_{x,x} + 2\psi_{y,y}\right),$$

$$\eta^{(1)}_{yyx} = \eta^{(1)}_{yxy} = \eta^{(1)}_{xyy} = \frac{1}{15}\left(4u_{0,yy} - 3u_{0,xx} + 8v_{0,xy}\right) - \frac{1}{15}z\left(8\psi_{y,xy} + 4\psi_{x,yy} - 3\psi_{x,xx}\right),$$

$$\eta^{(1)}_{yyz} = \eta^{(1)}_{yzy} = \eta^{(1)}_{zyy} = \frac{1}{15}\left(4W_{0,yy} - W_{0,xx} + 2\psi_{x,x} - 8\psi_{y,y}\right),$$

$$\eta^{(1)}_{zzx} = \eta^{(1)}_{zxz} = \eta^{(1)}_{xzz} = -\frac{1}{15}\left(3u_{0,xx} + 2v_{0,xy} + u_{0,yy}\right) + \frac{1}{15}z\left(3\psi_{x,xx} + 2\psi_{y,xy} + \psi_{x,yy}\right),$$

$$\eta^{(1)}_{zzy} = \eta^{(1)}_{zyz} = \eta^{(1)}_{yzz} = -\frac{1}{15}\left(v_{0,xx} + 3v_{0,yy} + 2u_{0,xy}\right) + \frac{1}{15}z\left(\psi_{y,xx} + 3\psi_{y,yy} + 2\psi_{x,xy}\right),$$

$$\eta^{(1)}_{xyz} = \eta^{(1)}_{yzx} = \eta^{(1)}_{zxy} = \eta^{(1)}_{xzy} = \eta^{(1)}_{yxz} = \eta^{(1)}_{zyx} = \frac{1}{3}\left(W_{0,xy} - \psi_{x,y} - \psi_{y,x}\right),$$

References

[1] M. Bacciocchi, M. Eisenberger, N. Fantuzzi, F. Tornabene, E. Viola, Vibration analysis of variable thickness plates and shells by the generalized differential quadrature method, Compos. Struct. 156 (2016) 218–237.

[2] M. Singh, R. Gayen, Mathematical study on the potential flow past a vertical submerged flexible plate of non-uniform thickness, J. Fluids Struct. 116 (2023) 103795.

[3] V. Kumar, S.J. Singh, V.H. Saran, S.P. Harsha, Vibration response of the exponential functionally graded material plate with variable thickness resting on the orthotropic Pasternak foundation, Mech. Based Des. Struct. Mach. (2023) 1–28.

[4] H. Sazan, S. Piperno, M. Layani, S. Magdassi, H. Shpaisman, Directed assembly of nanoparticles into continuous microstructures by standing surface acoustic waves, J. Colloid Interface Sci. 536 (2019) 701–709.

[5] S. Liu, E. Guo, V.M. Levin, F. Liu, Y.S. Petronyuk, Q. Zhang, Application of pulse acoustic microscopy technique for 3D imaging bulk microstructure of carbon fiber-reinforced composites, Ultrasonics 44 (2006) e1037–e1044.

[6] R. Resmi, V.S. Babu, M.R. Baiju, Impact of dimensionless length scale parameter on material dependent thermoelastic attenuation and study of frequency shifts of rectangular microplate resonators, in: IOP Conf. Ser. Mater. Sci. Eng., IOP Publishing, 2021, p. 12067.

[7] M.I. Hossain, M.S. Zahid, M.A. Chowdhury, M.M.M. Hossain, N. Hossain, MEMS-based energy harvesting devices for low-power applications–a review, Results Eng. (2023) 101264.

[8] A.C. Eringen, D. Edelen, On nonlocal elasticity, Int. J. Eng. Sci. 10 (1972) 233–248.

[9] A.C. Eringen, Linear theory of nonlocal elasticity and dispersion of plane waves, Int. J. Eng. Sci. 10 (1972) 425–435, https://doi.org/10.1016/0020-7225(72)90050-X.

[10] R.D. Mindlin, Microstructure in Linear Elasticity, Columbia Univ New York Dept Of Civil Engineering And Engineering Mechanics, 1963.

[11] D.C.C. Lam, F. Yang, A.C.M. Chong, J. Wang, P. Tong, Experiments and theory in strain gradient elasticity, J. Mech. Phys. Solids 51 (2003) 1477–1508, https://doi.org/10.1016/S0022-5096(03)00053-X.

[12] F. Yang, A.C.M. Chong, D.C.C. Lam, P. Tong, Couple stress based strain gradient theory for elasticity, Int. J. Solids Struct. 39 (2002) 2731–2743, https://doi.org/10.1016/S0020-7683(02)00152-X.

[13] C.W. Lim, G. Zhang, J.N. Reddy, A higher-order nonlocal elasticity and strain gradient theory and its applications in wave propagation, J. Mech. Phys. Solids 78 (2015) 298–313, https://doi.org/10.1016/j.jmps.2015.02.001.

[14] A.C. Eringen, J.L. Wegner, Nonlocal continuum field theories, Appl. Mech. Rev. 56 (2003) B20–B22.

[15] M. Hosseini, A. Jamalpoor, Analytical solution for thermomechanical vibration of double-viscoelastic nanoplate-systems made of functionally graded materials, J. Therm. Stress. 38 (2015) 1428–1456, https://doi.org/10.1080/01495739.2015.1073986.

[16] P.R. Saffari, S.O. Ismail, C. Thongchom, S. Sirimontree, T. Jearsiripongkul, Effect of magnetic field on vibration of electrorheological fluid nanoplates with FG-CNTRC layers, J. Vib. Eng. Technol. (2023) 1–20.
[17] R.D. Mindlin, N.N. Eshel, On first strain-gradient theories in linear elasticity, Int. J. Solids Struct. 4 (1968) 109–124.
[18] a. Jamalpoor, M. Hosseini, Biaxial buckling analysis of double-orthotropic microplate-systems including in-plane magnetic field based on strain gradient theory, Compos. Part B Eng. 75 (2015) 53–64, https://doi.org/10.1016/j.compositesb.2015.01.026.
[19] B.E. Yapanmış, Nonlinear vibration and internal resonance analysis of microbeam with mass using the modified coupled stress theory, J. Vib. Eng. Technol. 11 (2023) 2167–2180.
[20] Y. Zarabimanesh, P. Roodgar Saffari, P. Roudgar Saffari, N. Refahati, Hygro-thermo-mechanical vibration of two vertically aligned single-walled boron nitride nanotubes conveying fluid, J. Vib. Control 28 (2022) 2101–2120.
[21] S. Ajori, A.R. Eftekharfar, Buckling behavior of T-carbon nanobeams and nanoplates: a molecular dynamics study, Phys. B Condens. Matter. (2023) 415347.
[22] M. Balak, S. Jafari Mehrabadi, H. Mohseni Monfared, H. Feizabadi, Free vibration behavior of an elliptical sandwich microplate, consisting of a saturated porous core and two piezoelectric face layers, standing on an elastic foundation, Acta Mech. 233 (2022) 3253–3290.
[23] P.T. Hung, C.H. Thai, P. Phung-Van, Isogeometric bending and free vibration analyses of carbon nanotube-reinforced magneto-electric-elastic microplates using a four variable refined plate theory, Comput. Struct. 287 (2023) 107121.
[24] K. Khorshidi, B. Soltannia, M. Karimi, M. Zakaryaei, Natural frequencies of submerged microplate structures, coupled to stationary fluid, using modified strain gradient theory, Compos. Struct. (2023) 117583.
[25] H.B. Khaniki, M.H. Ghayesh, Airy stress based nonlinear forced vibrations and internal resonances of nonlocal strain gradient nanoplates, Thin-Walled Struct. 192 (2023) 111147.
[26] C. Dangi, R. Lal, Nonlinear thermal effect on free vibration of FG rectangular mindlin nanoplate of bilinearly varying thickness via Eringen's nonlocal theory, J. Vib. Eng. Technol. 10 (2022) 2979–2997.
[27] P.R. Saffari, C. Thongchom, T. Jearsiripongkul, P.R. Saffari, S. Keawsawasvong, S. Kongwat, Porosity-dependent wave propagation in multi-directional functionally graded nanoplate with nonlinear temperature-dependent characteristics on Kerr-type substrate, Int. J. Thermofluids 20 (2023) 100408.
[28] P. Phung-Van, A.J.M. Ferreira, H. Nguyen-Xuan, C.H. Thai, Scale-dependent nonlocal strain gradient isogeometric analysis of metal foam nanoscale plates with various porosity distributions, Compos. Struct. 268 (2021) 113949.
[29] P.T. Hung, P. Phung-Van, C.H. Thai, Small scale thermal analysis of piezoelectric–piezomagnetic FG microplates using modified strain gradient theory, Int. J. Mech. Mater. Des. (2023) 1–23.
[30] Z. Yang, H. Lu, S. Sahmani, B. Safaei, Isogeometric couple stress continuum-based linear and nonlinear flexural responses of functionally graded composite microplates with variable thickness, Arch. Civ. Mech. Eng. 21 (2021) 1–19.
[31] P.T. Hung, P. Phung-Van, C.H. Thai, A refined isogeometric plate analysis of porous metal foam microplates using modified strain gradient theory, Compos. Struct. 289 (2022) 115467.
[32] A. Reichardt, A.A. Shapiro, R. Otis, R.P. Dillon, J.P. Borgonia, B.W. McEnerney, P. Hosemann, A.M. Beese, Advances in additive manufacturing of metal-based functionally graded materials, Int. Mater. Rev. 66 (2021) 1–29.
[33] M. Ostolaza, J.I. Arrizubieta, A. Lamikiz, S. Plaza, N. Ortega, Latest developments to manufacture metal matrix composites and functionally graded materials through AM: a state-of-the-art review, Materials (Basel) 16 (2023) 1746.
[34] P.R. Saffari, S. Sirimontree, C. Thongchom, T. Jearsiripongkul, P.R. Saffari, S. Keawsawasvong, Effect of uniform and nonuniform temperature distributions on sound transmission loss of double-walled porous functionally graded magneto-electro-elastic sandwich plates with subsonic external flow, Int. J. Thermofluids (2023) 100311.
[35] S. Sirimontree, C. Thongchom, P.R. Saffari, N. Refahati, P.R. Saffari, T. Jearsiripongkul, S. Keawsawasvong, Effects of thermal environment and external mean flow on sound transmission loss of sandwich functionally graded magneto-electro-elastic cylindrical nanoshell, Eur. J. Mech. 97 (2023) 104774.
[36] C. Thongchom, P.R. Saffari, N. Refahati, P.R. Saffari, H. Pourbashash, S. Sirimontree, S. Keawsawasvong, An analytical study of sound transmission loss of functionally graded sandwich cylindrical nanoshell integrated with piezoelectric layers, Sci. Rep. 12 (2022) 1–16.
[37] P. Roodgar Saffari, W. Sher, C. Thongchom, Size dependent buckling analysis of a FG-CNTRC microplate of variable thickness under non-uniform biaxial compression, Buildings 12 (2022) 2238.
[38] C. Thongchom, P. Roodgar Saffari, P. Roudgar Saffari, N. Refahati, S. Sirimontree, S. Keawsawasvong, S. Titotto, Dynamic response of fluid-conveying hybrid smart carbon nanotubes considering slip boundary conditions under a moving nanoparticle, Mech. Adv. Mater. Struct. 30 (2023) 2135–2148.
[39] P. Phung-Van, Q.X. Lieu, H. Nguyen-Xuan, M. Abdel Wahab, Size-dependent isogeometric analysis of functionally graded carbon nanotube-reinforced composite nanoplates, Compos. Struct. 166 (2017) 120–135, https://doi.org/10.1016/J.COMPSTRUCT.2017.01.049.
[40] A. Hassaine, A. Mahi, Effects of graphene-platelets reinforcement on the free vibration, bending, and buckling of porous functionally-graded metal-ceramic plates, J. Compos. Mater. 57 (2023) 3909–3930.
[41] L. Zhang, Z. Xu, M. Gao, R. Xu, G. Wang, Static, dynamic and buckling responses of random functionally graded beams reinforced by graphene platelets, Eng. Struct. 291 (2023) 116476.
[42] Y. Wang, C. Feng, Z. Zhao, F. Lu, J. Yang, Torsional buckling of graphene platelets (GPLs) reinforced functionally graded cylindrical shell with cutout, Compos. Struct. 197 (2018) 72–79.
[43] R. Bahaadini, A.R. Saidi, Aeroelastic analysis of functionally graded rotating blades reinforced with graphene nanoplatelets in supersonic flow, Aerosp. Sci. Technol. 80 (2018) 381–391.
[44] S.K. Singh, M.K. Singh, P.P. Kulkarni, V.K. Sonkar, J.J.A. Grácio, D. Dash, Amine-modified graphene: thrombo-protective safer alternative to graphene oxide for biomedical applications, ACS Nano 6 (2012) 2731–2740.
[45] N.V. Nguyen, J. Lee, On the static and dynamic responses of smart piezoelectric functionally graded graphene platelet-reinforced microplates, Int. J. Mech. Sci. 197 (2021) 106310.
[46] P. Phung-Van, Q.X. Lieu, A.J.M. Ferreira, C.H. Thai, A refined nonlocal isogeometric model for multilayer functionally graded graphene platelet-reinforced composite nanoplates, Thin-Walled Struct. 164 (2021) 107862.
[47] Y.F. Zhang, L. Ma, W. Zhang, X.J. Gu, Nonlinear dynamic responses of functionally graded graphene platelet reinforced composite cantilever rotating warping plate, Appl. Math. Model. 113 (2023) 44–70.
[48] P. Phung-Van, H. Nguyen-Xuan, C.H. Thai, Nonlocal strain gradient analysis of FG GPLRC nanoscale plates based on isogeometric approach, Eng. Comput. 39 (2023) 857–866.
[49] P.R. Saffari, S. Sirimontree, C. Thongchom, T. Jearsiripongkul, P.R. Saffari, S. Keawsawasvong, S. Kongwat, Free and forced vibration of sandwich FGM porous variable thickness nanoplates integrated with magneto-electro-elastic layers via nonlocal strain gradient theory, Eng. Sci. (2023).
[50] C.H. Thai, A.J.M. Ferreira, P. Phung-Van, Size dependent free vibration analysis of multilayer functionally graded GPLRC microplates based on modified strain gradient theory, Compos. Part B Eng. 169 (2019) 174–188.
[51] P. Jafari, Y. Kiani, Free vibration of functionally graded graphene platelet reinforced plates: a quasi 3D shear and normal deformable plate model, Compos. Struct. 275 (2021) 114409.
[52] M. Hosseini, M. Bahreman, A. Jamalpoor, Using the modified strain gradient theory to investigate the size-dependent biaxial buckling analysis of an orthotropic multi-microplate system, Acta Mech. (2016), https://doi.org/10.1007/s00707-016-1570-0.
[53] P.R. Saffari, C. Thongchom, T. Jearsiripongkul, P.R. Saffari, S. Keawsawasvong, S. Kongwat, Thermo-vibro-acoustic analysis of pavement under a harmonically rectangular moving load, Int. J. Thermofluids 20 (2023) 100409.
[54] M. Xu, X. Li, Y. Luo, G. Wang, Y. Guo, T. Liu, J. Huang, G. Yan, Thermal buckling of graphene platelets toughening sandwich functionally graded porous plate with temperature-dependent properties, Int. J. Appl. Mech. 12 (2020) 2050089.
[55] G. Cowper, The shear coefficient in Timoshenko's beam theory, J. Appl. Mech. 33 (1966) 335–340.
[56] L. Hadji, M. Avcar, Ö. Civalek, An analytical solution for the free vibration of FG nanoplates, J. Brazilian Soc. Mech. Sci. Eng. 43 (2021) 1–14.
[57] Z. Xu, Q. Huang, Vibro-acoustic analysis of functionally graded graphene-reinforced nanocomposite laminated plates under thermal-mechanical loads, Eng. Struct. 186 (2019) 345–355.
[58] A. Gupta, N.K. Jain, R. Salhotra, P.V. Joshi, Effect of crack location on vibration analysis of partially cracked isotropic and FGM micro-plate with non-uniform thickness: an analytical approach, Int. J. Mech. Sci. 145 (2018) 410–429.
[59] S. Thai, H.-T. Thai, T.P. Vo, V.I. Patel, Size-dependant behaviour of functionally graded microplates based on the modified strain gradient elasticity theory and isogeometric analysis, Comput. Struct. 190 (2017) 219–241.
[60] M. Arefi, E.M.-R. Bidgoli, R. Dimitri, F. Tornabene, Free vibrations of functionally graded polymer composite nanoplates reinforced with graphene nanoplatelets, Aerosp. Sci. Technol. 81 (2018) 108–117.